Journal of Geophysical Research: Atmospheres

RESEARCH ARTICLE
10.1029/2018JD028545

Quantification of Precipitation Asymmetries of Tropical Cyclones Using 16-Year TRMM Observations

Yongxian Pei[1] **and Haiyan Jiang**[1]

[1]Department of Earth and Environment, Florida International University, Miami, FL, USA

Key Points:
- Wavenumber 1 only contributes 37% of total perturbation energy of tropical cyclone precipitation, while the sum of wavenumbers 1 through 6 contributes over 70%
- Maximum motion-relative wavenumber 1 rainfall asymmetry is down motion but shifts cyclonically around storm center after adding wavenumber 2-6 components
- Shear effect is dominant over motion and a downshear left asymmetry maximum is found regardless of shear direction to motion, shear magnitude, and motion speed

Correspondence to:
H. Jiang,
haiyan.jiang@fiu.edu

Citation:
Pei, Y., & Jiang, H. (2018). Quantification of precipitation asymmetries of tropical cyclones using 16-year TRMM observations. *Journal of Geophysical Research: Atmospheres*, *123*, 8091–8114. https://doi.org/10.1029/2018JD028545

Received 19 FEB 2018
Accepted 6 JUL 2018
Accepted article online 12 JUL 2018
Published online 3 AUG 2018

Abstract Both low and higher wavenumber asymmetries of tropical cyclone (TC) precipitation are quantified from 16 years of Tropical Rainfall Measuring Mission (TRMM) microwave imager rainfall estimates using Fourier decomposition. The energy spectrum of rainfall perturbation and impacts of the storm motion and vertical wind shear to the rainfall asymmetry are analyzed. It is found that the wavenumber 1 perturbation only contributes 37% of the total perturbation energy of total TC precipitation, while over 70% of the total perturbation energy is from the sum of wavenumbers 1 through 6. Most of the total precipitation asymmetry is from the heavy precipitation, and contributions for light and moderate precipitation types are small. The maximum motion-relative precipitation asymmetry is generally located down motion but shifts cyclonically after adding wavenumber 2–6 components to wavenumber 1. The asymmetry index of wavenumber 1 and 1–6 asymmetries relative to the vertical wind shear is about 2 to 3 times as large as that relative to the storm motion. The vertical wind shear is a more important factor than the storm motion in producing precipitation asymmetry, especially for the wavenumber 1. A dominant downshear left wavenumber-1 asymmetry maximum is found regardless of the shear vector orientation to the TC motion, the magnitude of the shear value, and the speed of TC motion. However, the maximum asymmetry of wavenumber 1–6 asymmetry becomes downshear right for the subgroup with low shear, fast motion, and the shear vector left to the motion.

1. Introduction

Several studies have investigated the influence of storm motion (Burpee & Black, 1989; Frank, 1977; Lonfat et al., 2004; Marks, 1985; Miller, 1958; Rodgers et al., 1994) and vertical wind shear (Cecil, 2007; Corbosiero & Molinari, 2002; Wingo & Cecil, 2010) on the asymmetries present in the rainfall distribution in tropical cyclones (TCs). While studies have most often analyzed these effects separately, only a few studies have addressed the combined effect of storm motion and vertical wind shear on TC precipitation asymmetries (Chen et al., 2006; Corbosiero & Molinari, 2003; Rogers et al., 2003; Ueno, 2007). Likewise, these studies have typically focused on only the wavenumber 1 contribution to rainfall asymmetry.

Due to the lack of quantitative measurements of TC rainfall and environmental wind shear over the open ocean, earlier research focused on the effect of storm motion on TC rainfall asymmetry using different approaches such as case studies (e.g., Burpee & Black, 1989; Marks, 1985; Miller, 1958; Reasor et al., 2000; Willoughby et al., 1984), statistical methods applied to a small sample size (Frank, 1977; Rodgers et al., 1994), or numerical modeling (Frank & Ritchie, 1999; Shapiro, 1983). These studies agree that the rainfall maximum in the inner core region is generally observed in down motion quadrants, which indicates the importance of frictional convergence in the boundary layer, particularly to the right of motion (Frank & Ritchie, 1999; Shapiro, 1983). Whereas the approach prior typically focused on case studies, Lonfat et al. (2004, hereafter LMC04) were among the first to verify the down motion and right of motion rainfall maxima using a larger sample of storms (260; 2,121 instantaneous precipitation observations from 1998 to 2000). Their methodology consisted of analyzing motion-relative composites of the Fourier decomposed wavenumber 1 distribution of passive microwave-derived surface rain rate estimates from the Tropical Rainfall Measuring Mission (TRMM) microwave imager (TMI).

Similar to the storm motion relative rainfall asymmetry, studies examining the shear-relative rainfall distribution agree that the wavenumber 1 asymmetry consists of a downshear rainfall maximum. These studies arrived at a similar conclusion despite using a variety of datasets. For example, Corbosiero and Molinari (2002) analyzed lightning data from the National Lightning Detection Network (NLDN) to investigate the asymmetry of convection relative to the vertical wind shear at varying radii from the center. They showed

that more than 90% of flashes occurred in the downshear left quadrant within a radius of 300 km. When differentiated by only those within 100 km the preferred location is slightly downshear left, while between 100 and 300 km the preference shifted to the downshear right. Cecil (2007) similarly found a downshear left maximum using multipassive microwave sensor-derived rain rates from the Remote Sensing Systems retrievals for a large sample of Atlantic storms (1998–2004). Using an improved version of the Remote Sensing Systems retrieval, with degraded resolution, Wingo and Cecil (2010) extended Cecil's (2007) study globally and further concluded that the majority of the asymmetry in mean rain rates is accounted for by the heaviest rain rates.

Considering that the storm motion and vertical wind shear both create rainfall asymmetries in TCs, one of the most important questions is which effect is dominant. Corbosiero and Molinari (2003) investigated the combined effect of shear and motion by using the same National Lightning Detection Network data set as Corbosiero and Molinari (2002). They observed that the front-right quadrant favored by storm motion and the downshear left quadrant favored by shear often overlap in their sample. By examining subsets where motion and shear favor opposing regions, they found that the environmental shear is the dominant factor modulating the convective activity in hurricanes. In a high-resolution, cloud-resolving numerical model simulation of Hurricane Bonnie (1998), Rogers et al. (2003) also investigated the combined contributions of vertical wind shear and motion to rainfall asymmetry. They found that an along-track shear resulted in a symmetric rainfall accumulation, whereas a cross-track shear created a right-side asymmetry in the accumulated rainfall.

Using the same TRMM data set and Fourier decomposition method as LMC04, Chen et al. (2006, hereafter CKM06) verified the conclusion of Corbosiero and Molinari (2003) that the vertical wind shear dominates the amplitude of the wavenumber 1 rainfall asymmetries relative to the effect of motion, particularly in a moderate to highly sheared environment (where the asymmetry is predominately downshear left). In a low shear environment, the asymmetry from storm motion had a larger contribution, especially in the outer rainband regions. Similar to CKM06, Ueno (2007) found that the magnitude of asymmetry was greatest when the shear vector and storm motion vector were oriented in the same direction or when the shear vector was right to the motion vector.

Although the wavenumber 1 asymmetry appears to be dominant, a few studies (CKM06; Reasor et al., 2009; Yu et al., 2015; Zhu et al., 2014) have also suggested that perturbations due to higher wavenumbers (>1) may also have potentially significant contributions. For example, in a numerical modeling study Zhu et al. (2014) showed that the energy from wavenumbers 1 to 6 contributed a large amount of energy to the total perturbation field of potential vorticity, while CKM06 also found that, though wavenumber 1 is dominant, the wavenumber 2 rainfall asymmetry still contributes half of the amplitude of wavenumber 1 asymmetry.

This study will complement the previous studies by utilizing the Fourier decomposition method on a large sample of satellite-derived rain rates to quantify TC precipitation asymmetries with respect to both storm motion and vertical wind shear. Given the relative lack of studies examining the contributions of higher wavenumbers, in this study, we focus on the rainfall asymmetry component not only from wavenumber 1 but higher wavenumbers (up to 6). In addition to the total precipitation, we will also uniquely analyze the asymmetry of three categorized rain rates: light, moderate, and heavy precipitation. The 16 years of TRMM observations of TC inner cores utilized in this study is likely, to date, the most robust data set utilized to examine the TC precipitation distribution. Using this long-term data set, we will attempt to answer the following questions:

In the energy spectrum

1. How much do higher wavenumbers contribute to the total perturbation energy of TC precipitation compared to the wavenumber 1?

In both a motion-relative and shear-relative frameworks

1. How much do higher wavenumbers contribute to the amplitude of asymmetry compared to the wavenumber 1?
2. Do higher wavenumber asymmetry components change the location of maximum precipitation?
3. How is the maximum asymmetry amplitude and location sensitive to varying storm motion speeds and vertical wind shear magnitudes?

Table 1
Numbers and Percentages (in Parentheses) of Selected TMI Overpasses for Different Intensity Stages in Different Basins

	ATL	EPA	NWP	NIO	SIO	SPA	TOTAL
TS	519 (62.0)	372 (65.6)	511 (45.9)	79 (79.8)	412 (62.5)	160 (59.9)	2053 (58.0)
CAT 1-2	235 (28.1)	122 (21.5)	360 (32.4)	13 (13.1)	161 (24.4)	57 (21.4)	948 (26.8)
CAT 3-5	83 (9.9)	73 (12.9)	242 (21.7)	7 (7.1)	86 (13.1)	50 (18.7)	541 (15.2)
TOTAL	837 (23.6)	567 (16.0)	1113 (31.4)	99 (2.8)	659 (18.6)	267 (7.6)	3542

Under the combined effects of shear and motion

1. When does vertical wind shear dominate the TC inner core precipitation distribution over motion, and vice versa?

2. Data and Method

2.1. Date Sources

The data set used in this study is 16-year (1998–2013) TRMM TMI data from the TRMM Tropical Cyclone Precipitation Feature (TCPF) database (Jiang et al., 2011). The TRMM TCPF database includes TRMM overpasses of all global TCs that reached at least tropical storm (TS) intensity during their lifetimes. TCs were separated into six oceanic basins, including Atlantic (ATL), East Pacific (EPA), northwest Pacific (NWP), North Indian Ocean (NIO), South Indian Ocean (SIO), and South Pacific Ocean (SPA). The storm center, intensity, and storm motion speed and direction of each overpass were interpolated from the best track data. The best track data of ATL and EPA basins were obtained from the National Hurricane Center hurricane database (HURDAT2). For the rest of the basins, the best track data were from the U.S. Navy's Joint Typhoon Warning Center. Based on the maximum sustained wind speed (V_{max}) at the TRMM observation time, all TC overpasses were classified into tropical depression ($V_{max} < 34$ kt), TSs (34 kt $\leq V_{max} < 64$ kt), category 1–2 hurricanes (CAT1-2; 64 kt $\leq V_{max} \leq 95$ kt), and category 3–5 hurricanes (CAT3-5; $V_{max} > 95$ kt) according to the Saffir-Simpson Hurricane Scale.

The best track interpolated storm centers for TS, CAT1-2, and CAT3-5 overpasses were manually adjusted by Zagrodnik and Jiang (2014) and Tao et al. (2017) in order to better align with the representation of the TRMM Precipitation Radar and/or TMI 37-GHz channel. Sometimes the best track interpolated center could be off the real center by a certain distance ranging from a few kilometers to tens of kilometers. Therefore, the manually recentered data set is critical to the success of the Fourier transform wavenumber decomposition performed in this study. Tropical depression overpasses are not included in this study due to difficulties of center fixing for these low intensity storms.

The TMI has an 878-km swath (760 km before the TRMM orbital boost in August 2001), which is much wider than the TRMM radar's swath width. But still, not all TMI overpasses provided a good coverage for the TC observation. In this study, we select overpasses by using the criterion of capturing the entire inner 200-km radius from the storm center. We also require that the TC had to remain over water and did not undergo extratropical transition within a future 24-hr period. The *extratropical transition* is defined by the best track data of HURDAT2 (https://www.nhc.noaa.gov/data/). Only Atlantic and Eastern Pacific Ocean incorporated extratropical transition in the best track data. In our study, we excluded the overpasses found in extratropical transition cycle. Finally, 3,542 qualified TC overpasses are selected including 2,053 TS, 948 CAT1-2, and 541 CAT3-5 overpasses. Table 1 shows the sample sizes for six different basins and three different intensity stages.

The TMI surface rainfall estimates from version 7 (V7) of the TMI 2A12 algorithm (Kummerow et al., 2001; Olson et al., 1996) are used in this study. The 2A12 rainfall algorithm retrieves surface rainfall using TMI frequencies (10, 19, 21, 37, and 85 GHz) based on the Goddard Profiling algorithm (Kummerow et al., 2001), which used a Bayesian approach to retrieve surface rain. Using a numerical cloud model, a large data set of precipitation profiles was generated. Brightness temperatures associated with each simulated profile were calculated using a radiative transfer model. By comparing the observed and model calculated brightness

Table 2
Mean Values of Current TC Intensity V_{max}, Vertical Wind Shear Magnitude, Storm Motion Speed and Numbers and Percentages (in Parentheses) of Selected TMI Overpasses With Shear Same as, Opposite to, to the Left of, and to the Right of Motion for the Total Data Set, Different Oceanic Basins, and Different Intensity Stages

	V_{max}	Shear	Motion	Same	Opposite	Left	Right
ATL	61.4	10.6	5.2	104 (12.4)	106 (12.7)	155 (18.5)	472 (56.4)
EPA	60.6	6.1	4.6	80 (14.1)	52 (9.2)	246 (43.4)	189 (33.3)
NWP	72.2	7.9	5.2	166 (14.9)	95 (8.5)	398 (35.8)	454 (40.8)
NIO	51.1	10.3	3.2	26 (26.3)	3 (3.0)	40 (40.4)	30 (30.3)
SIO	60.9	8.9	3.9	120 (18.2)	43 (6.5)	358 (54.4)	138 (20.9)
SPA	65.2	10.1	4.6	56 (21.0)	22 (8.2)	142 (53.2)	47 (17.6)
TS	45.6	9.1	4.6	282 (13.7)	206 (10.0)	619 (30.2)	946 (46.1)
CAT1-2	77.5	8.6	4.9	184 (19.4)	65 (6.9)	244 (25.7)	455 (48.0)
CAT3-5	114	6.9	5	86 (15.9)	50 (9.2)	161 (29.8)	244 (45.1)
Total	64.5	8.7	4.8	552(15.6)	321 (9.1)	1024 (28.9)	1645 (46.4)

Note. For the last four rows for different intensity stages, shear directions of Southern Hemisphere overpasses are flipped around the motion direction to be consistent with the Northern Hemisphere frame of reference.

temperatures, the probability that if a simulated profile is likely to be as realistic as an observed profile was calculated. The model profiles were then weighted and summed to composite the best estimate profile of the observation, which was used to determine the rainfall estimate of each observed brightness temperature sets from all frequencies. The algorithm produces rain rates at a horizontal resolution of 5.1×5.1 km^2 (4.4×4.4 km^2 before August 2001 orbital boost).

In this study, the TMI 2A12 rain rate (R) is categorized into four precipitation types: total precipitation ($R \geq 0.5$ mm/hr), heavy precipitation ($R \geq 10$ mm/hr), moderate precipitation (10 mm/hr $> R \geq 5$ mm/hr), and light precipitation (5 mm/hr $> R \geq 0.5$ mm/hr). Jiang et al. (2011) used rain rate greater than 5 mm/hr to define *heavy rain*, which contributed to about 50%–60% of total volumetric rain in TCs. Wingo and Cecil (2010) shows that over a quarter degree grid ($0.25 \times 0.25°$), 8 mm/hr is a relatively *heavy* rain rate. Since the 2A12 rain rate product has a finer resolution than a quarter degree, we subjectively classify higher than 10 mm/hr as heavy rain rate, higher than 5 mm/hr and lower than 10 mm/hr as *moderate rain*, and lower than 5 mm/hr as *light rain*. Since the TMI V7 oceanic algorithm gives a high number of false positive rain rates, we use a threshold rain rate of 0.5 mm/hr with a probability 95% of rain as the minimum criterion of raining (Zagrodnik & Jiang, 2014).

One additional data set that supplements the TRMM TCPF database is included to calculate the magnitude and direction of the vertical wind shear. The wind field data are derived from the 0.75° resolution European Centre for Medium-Range Weather Forecasts interim reanalysis data set (Simmons et al. 2006). The vertical wind shear is calculated as the difference between the averaged wind vectors at the 200- and 850-hPa levels. Following Zagrodnik and Jiang (2014) and Tao et al. (2017), the wind vectors are averaged within a ring of 500–750 km from the TC center to eliminate the influence of the storm's circulation as much as possible. As tested by Wingo and Cecil (2010), the rainfall distribution does not appear to be sensitive to the depth of the vertical wind shear calculation, that is, over the deep layer (200–850 hPa) or shallow layer (500–850 or 700–925 hPa). Therefore, we will only use the deep-layer shear calculation.

In Table 2 the mean values of TC intensity, motion speed, and vertical wind shear magnitudes are shown for the six basins and three intensity groups, respectively. Among the six basins, the average intensity of NWP TC overpasses is the highest. The average intensity of NIO is the lowest. The overall average intensities of the six basins are about 60 kt. The motion speeds of all basins are in the range from 3 to 5 m/s. NIO overpasses have the lowest motion speed. The average shear magnitudes of ATL, NIO, and SPA overpasses are about 10 m/s, which are higher than those of EPA, NWP, and SIO. Among the three intensity groups, it is noteworthy that TS overpasses have the highest average wind shear magnitude and lowest motion speed. CAT3-5 overpasses have the lowest average wind shear magnitude and highest motion speed.

2.2. Analysis Method

Similar to LMC04, CKM06, and Yu et al. (2015), the TC rainfall asymmetry is quantified by using Fourier decomposition. Within a polar coordinate system using the TC center as the origin, the spatial asymmetries of rainfall are computed by binning TMI rain rates in 10-km-wide annuli from 30-km radius to 200-km radius from the TC center. In each annulus, the Fourier coefficients are computed using the following equations (Stull, 1987):

$$a_n = \frac{1}{N}\sum_{k=0}^{N-1} R(k)\cos\left(\frac{2\pi nk}{N}\right), \tag{1}$$

$$b_n = -\frac{1}{N}\sum_{k=0}^{N-1} R(k)\sin\left(\frac{2\pi nk}{N}\right), \tag{2}$$

where *R(k)* is each of the individual rain rate estimates and *n* is the wavenumber. *N* is equal to 360, which is the total number of points being analyzed in each annulus. *N* is also the highest wavenumber that we can resolve in this Fourier decomposition; *k* is the index of each point; *i* is the imaginary unit, which is defined by its property $i^2 = -1$. The complex formula of Fourier coefficient c_n is

$$c_n = a_n + ib_n, \tag{3}$$

Previous studies have argued on whether the asymmetric deep convection (asymmetric perturbation energy) or the widespread, symmetric shallow-to-moderate precipitation is more important to TC intensification. One side emphasizes the importance of asymmetric deep convection such as hot towers and convective bursts (Montgomery et al., 2006; Montgomery & Smith, 2011). However, the other side emphasizes the symmetric mechanism for TC intensification (Nolan et al., 2007; Ooyama, 1969; Shapiro & Willoughby, 1982) arguing that the azimuthally averaged latent heating release is much more important for the vortex intensification than asymmetric heating. According to Zhu et al. (2014), the total rainfall asymmetric perturbation energy through all wavenumbers can be represented as

$$\sigma_\eta^2 = \sum_{n=1}^{N-1} |c(n)|^2. \tag{4}$$

Then the fractional contribution of each wavenumber *n* to the total perturbation energy (*E(n)*) is

$$E(n) = \frac{|c_n|^2}{\sigma_\eta^2}. \tag{5}$$

We can also call *E*(*n*) as the normalized perturbation energy spectrum. Clearly, *E*(*n*) provides a way to quantify the contribution of a certain wavenumber to the total perturbation energy as a percentage. By definition, summing *E*(*n*) through all wavenumbers will reach unity

$$\sum_{n=1}^{N-1} E(n) = 1, \tag{6}$$

The rainfall asymmetric component of wavenumber *n*, R_n, can be represented by

$$R_n = a_n\cos\left(\frac{2\pi nk}{N}\right) - b_n\sin\left(\frac{2\pi nk}{N}\right), \tag{7}$$

Note that R_n is not divided by the azimuthal mean rain rate (wavenumber 0, R_0) as used in LMC04. Instead, we will compare the unnormalized amplitudes of wavenumber 1 and the sum of wavenumber 1 through wavenumber 6 rainfall components in mm/hr (R_1 and $R_{1\text{-}6}$) and normalized percentages (R_1/R_0 and $R_{1\text{-}6}/R_0$) in the

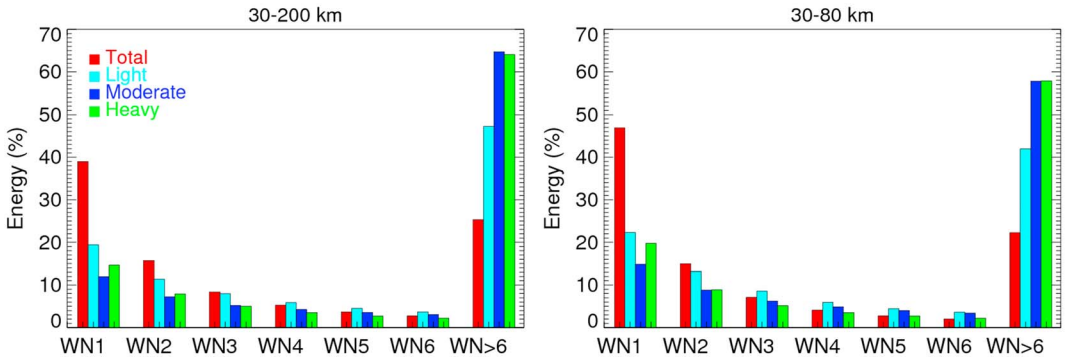

Figure 1. The percentage of total perturbation energy contributed by wavenumbers (WN) 1–6 and > 6 perturbations averaged over the annulus from 0 to 200 km and from 30 to 80 km from the TC center for total precipitation, light precipitation, moderate precipitation, and heavy precipitation, respectively.

composite 2-D distribution of Figure 4, respectively. In the composite 2-D figures (Figures 5–13) following Figure 4, only the normalized asymmetry components in percentages (R_1/R_0 or $R_{1\text{-}6}/R_0$) will be shown.

When the motion-relative rainfall asymmetries are concerned, the rainfall asymmetry is composited relative to the motion vector over each TMI overpass. We stratify the motion speed into two categories: slow motion (motion speed $<$5 m/s) and fast motion (motion speed $\geq$5 m/s). When the shear-relative rainfall asymmetries are concerned, the rainfall asymmetry is composited relative to the shear vector over each TMI overpass. We stratify the shear magnitude into three categories: low shear (0–5 m/s), moderate shear (5–10 m/s), and high shear ($>$10 m/s). When the combined effect of both motion and shear is concerned, we follow CKM06's methodology to stratify the shear and motion vector angle difference (dA = shear angle—motion angle) into four categories: the shear vectors are in the same (d$A \leq 22.5°$), opposite (d$A \geq 157.5°$), right ($22.5° <$ d$A < 157.5°$), or left ($-157.5° <$ d$A < -22.5°$) of the storm motion directions. When we composite overpasses over all basins in Figures 4, 7, 8, and 11–15, the Southern Hemisphere (SH) overpasses are mirrored relative to either the shear or the motion direction to a Northern Hemisphere (NH) frame of reference to account for the Coriolis effect as in CKM06. For both the motion-relative and shear-relative frameworks, the phase maximum represents the phase angle of the largest rainfall asymmetry. Also, as pointed by CKM06, "the larger the asymmetry amplitude, the more variability in the spatial distribution of TC rainfall may be explained by the reference system (either the environmental shear relative or the TC motion relative)."

Table 2 shows numbers and percentages of overpasses of four categories of different shear orientations relative to the motion direction. Since the angle difference in the *same* and *opposite* groups covers only half of the range as that in the *left* and *right* groups, we expect a smaller sample size in the first two groups. However, even with the same angle difference range, the same and opposite groups have different sample sizes. So do the left and right groups. Overall, for global basins after SH overpasses are mirrored there are more overpasses with the shear direction same as (15.6%) group than opposite to (9.1%) the TC motion direction. Overpasses with the shear direction to the right (46.4%) of the motion direction are almost twice as many as those to the left (28.9%). There are some variations for different basins. For example, the ATL basin has almost the same number of overpasses with shear same as or opposite to the motion direction, while all other basins have a higher number of overpasses with shear same as than those opposite to the motion direction. The EPA basin has more overpasses having the shear direction to the left of motion direction, while all other basins have more overpasses with the shear direction to the right (left in SIO and SPA basins) of motion direction. For the three intensity groups, it is always true that there are more overpasses with shear same as (right of) than those opposite to (left of) the motion direction.

3. Results

3.1. Rainfall Perturbation Energy Spectrum

Figure 1 shows the normalized energy spectrum of rainfall perturbations averaged within 30–200 km from the storm center and over the annulus from 30 to 80 km from the storm center. For the entire 30- to 200-

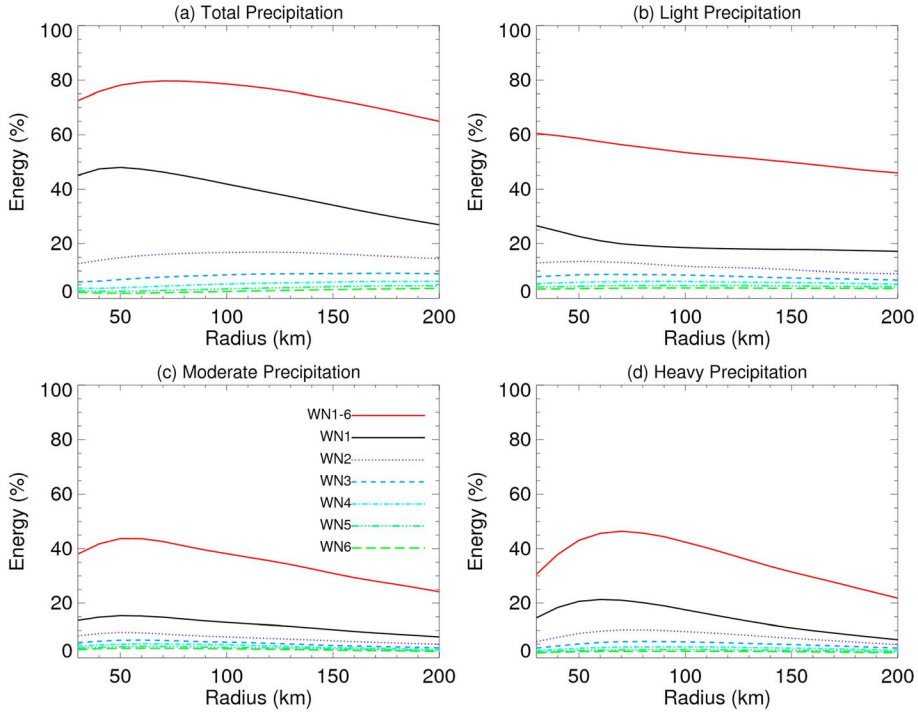

Figure 2. The percentage of total perturbation energy contributed by wavenumbers (WN) 1–6 and 1–6 (1 through 6) as a function of radial distance for (a) total precipitation, (b) light precipitation, (c) moderate precipitation, and (d) heavy precipitation.

km region, wavenumber 1 contributes 37% of the total perturbation energy of total precipitation, but only 19, 11, and 13% of the total perturbation energy of light, moderate, and heavy precipitation, respectively. This suggests that separating total precipitation into subcategories breaks perturbations down by producing larger higher wavenumber components. Comparing the contribution of wavenumber 1 with higher wavenumbers, it is found that the energy contribution decreases quickly as the wavenumber gets higher for all four precipitation categories. For example, the energy of wavenumber 1 is about double of wavenumber 2, which is about the double of wavenumber 3, so on and so forth. However, the sum of energies from wavenumber 2 through wavenumber 6 is similar to the energy of wavenumber 1 for the total precipitation. This sum is about 30% to 50% higher than the energy of wavenumber 1 for the light, moderate, and heavy precipitation. Therefore, by analyzing both R_1 and $R_{1\text{-}6}$ in this study, at least 70% of the total perturbation energy of total precipitation is covered. For the approximate eyewall region (from 30 to 80 km from the TC center), the wavenumber 1 contributes a much higher percentage to the total perturbation energy than for the entire 30- to 200-km region for all precipitation categories, especially for the total precipitation. As a result, the energy from wavenumbers higher than 6 is lower than that for the entire 30- to 200-km region.

As the energy spectrum can be different at various radii from the TC center, Figure 2 shows the percentage of total perturbation energy contributed by wavenumbers from 1 to 6, respectively, and the sum of wavenumber 1 through wavenumber 6 (wavenumbers 1–6) as a function of the radial distance. The wavenumber 1 energy is higher in the inner core region (within 30–100 km) than in the outer region for all four precipitation categories. Perturbation energies from wavenumber 2 and higher do not change much with the radial distance. As a result, the sum of energy from wavenumbers 1 to 6 is less in the outer region than in the inner region. For different precipitation types, the stronger the precipitation rate, the less the outer region perturbation energy is contributed by the wavenumber 1–6 energy. The peak energy contributions are located at where wavenumber 1–6 energy dominates the most.

Moderate and heavy precipitation types have more high wavenumber (higher than wavenumber 6) energy relative to light precipitation. As shown in Figure 1, the perturbation energy from wavenumbers >6

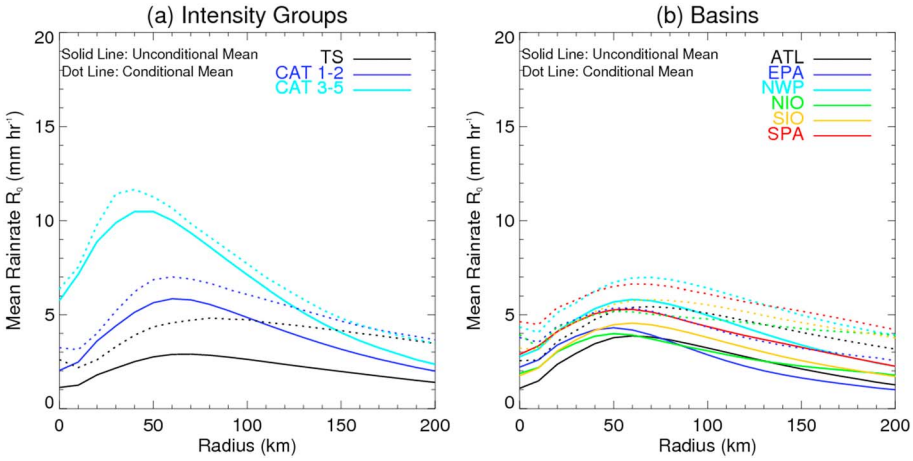

Figure 3. Mean rain rates (R_0) of total precipitation for (a) three different intensity stages, (b) six oceanic basins, and (c) mean rain rates (R_0) of light, moderate, and heavy precipitation.

contributes about 49% of the total perturbation energy of light precipitation within 30- to 200-km radius, but the contribution from wavenumbers >6 increases to 67% for moderate and heavy precipitation. From both Figures 1 and 2, we can see that the total precipitation has the highest energy contribution from wavenumbers 1 to 6, followed by the light precipitation. Both moderate and heavy precipitations have lower-energy contribution from wavenumbers 1 to 6 than the light precipitation. Stronger convection with moderate or heavy rain rates is usually small in size and distributed randomly distributed around the TC center (Tao & Jiang, 2015), which is the characteristic of higher wavenumbers. Tao and Jiang (2015) showed that the shallow precipitation is more symmetrically distributed around the TC center, which is the characteristic of lower wavenumbers.

3.2. Azimuthal Mean Rain Rate

TC rainfall asymmetry can be represented by the decomposed field of rain rates either normalized by the azimuthal mean rain rate (LMC04 and CKM06) or not (Yu et al., 2015). Before comparing the two representations of asymmetry, to understand the relative amplitude of the composited field to the mean rain rate, it is important to show how the azimuthal mean rain rates distribute radially among different intensity groups, basins, and precipitation categories (Figure 3). As expected, the unconditional mean rain rate, which takes the azimuthal average counting in the nonraining data points, is smaller than the conditional mean rain rate (without nonraining data points) in all radii. It is worth noting that the azimuthal unconditional mean rain rate is used to normalize wavenumber 1 or 1–6 asymmetry components in the current study as well as in LMC04 and CKM06. From Figure 3a, the peak unconditional mean rain rates are 3, 6, and 11 mm/hr for TS, CAT1-2, and CAT3-5 intensity groups, respectively. The average rain rate increases with radius until it reaches the peak and decreases outward. The location of the peak rain rate for TS, CAT1-2, and CAT3-5 intensity groups are at about 60, 60, and 40 km from the storm center, respectively. The radial rain rate distribution is consistent with LMC04 and Marks (1985). Unconditional mean rain rates are the highest for TCs in the NWP basin at all radii, while ATL TCs have the lowest unconditional mean rain rate in the inner 50-km region and EPA TCs have the lowest unconditional mean rain rate in the region from 50- to 200-km region from the storm center (Figure 3b). This is due to stronger storm intensity in WNP than other basins and is consistent with previous studies of TC rainfall climatology in different basins (Jiang et al., 2011; Jiang & Zipser, 2010).

3.3. Motion Effect

The 2-D motion-relative composites of unnormalized Fourier decomposed rainfall wavenumber 1 and 1–6 rainfall asymmetry components and those normalized by the azimuthal unconditional mean rain rate are shown in Figure 4. Figure 4l shows that the maximum of wavenumber 1 rainfall asymmetry component (R_1) is down motion or slightly down motion left at the radius of 100 km for total, moderate, and heavy

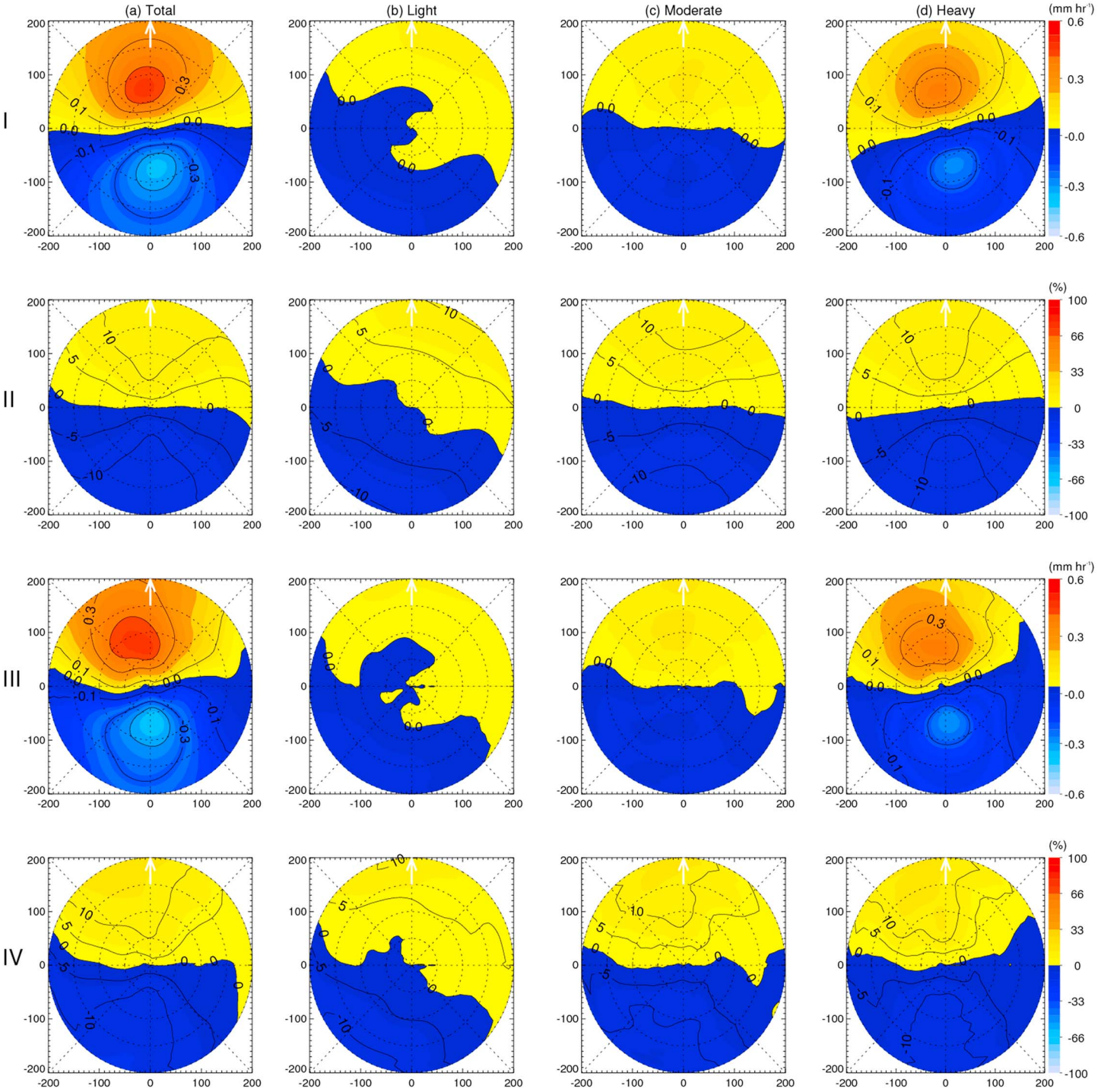

Figure 4. The composite motion-relative (I) unnormalized wavenumber 1 asymmetry (R_1, mm/hr), (II) normalized wavenumber 1 asymmetry (R_1/R_0, %), (III) unnormalized wavenumber 1–6 asymmetry ($R_{1\text{-}6}$, mm/hr), and (IV) normalized wavenumber 1-6 asymmetry ($R_{1\text{-}6}/R_0$, %) of (a) total precipitation, (b) light precipitation, (c) moderate precipitation, and (d) heavy precipitation. The white arrow (pointing upward) represents the orientation of motion vector. The color scale represents the amplitude of the unnormalized or normalized wavenumber 1 or 1–6 asymmetry. The red color responds to the maximum positive anomaly and the blue the minimum anomaly relative to the azimuthal mean rainfall. Dotted range rings represent the 50-, 100-, 150-, and 200-km radii. The contours in (I) and (III) delineate −0.3, −0.1, 0, 0.1, and 0.3 mm/hr rain rate. The contours in (II) and (IV) delineate the normalized asymmetry of −10%, −5%, 0, 5%, and 10%.

Table 3
The Asymmetry Index (AI) of the Composite Motion-Relative Unnormalized Wavenumber 1 Asymmetry (R_1, mm/hr), Normalized Wavenumber 1 Asymmetry (R_1/R_0, %), Unnormalized Wavenumber 1–6 Asymmetry ($R_{1\text{-}6}$, mm/hr), and Normalized Wavenumber 1–6 Asymmetry ($R_{1\text{-}6}/R_0$, %) of (a) Total Precipitation, (b) Light Precipitation, (c) Moderate Precipitation, and (d) Heavy Precipitation (Corresponding to Figure 4)

AI	(a) Total	(b) Light	(c) Moderate	(d) Heavy
R_1 (mm/hr)	0.21	0.02[a]	0.05[a]	0.16[a]
R_1/R_0 (%)	6.7	3.4[a]	5.9[a]	6.4[a]
$R_{1\text{-}6}$ (mm/hr)	0.22 (4.8%)	0.02 (0%)[a]	0.05 (0%)[a]	0.17 (11.8%)[a]
$R_{1\text{-}6}/R_0$ (%)	6.7 (0%)	3.3 (−2.9%)[a]	6.0 (1.7%)[a]	7.1 (10.9%)[a]

Note. The percentage in each pair of parentheses represents the percentage increase of the asymmetry index from R_1 to $R_{1\text{-}6}$ or from R_1/R_0 to $R_{1\text{-}6}/R_0$.
[a]The statistical significance of the value from the value in column (a) at the 99.9% confidence level.

precipitation types. For the light precipitation, the R_1 maximum is located right of motion in the storm inner core region and down motion in the storm outer region. In this study, we roughly refer to within 100-km radius as the inner core region and between 100- and 200-km radius as the outer region by following DeMaria et al. (2012) and Jiang et al. (2013). After normalizing by the azimuthal unconditional mean rain rate at each annulus, Figure 4II shows that the phase maximum of R_1/R_0 is still down motion for total, moderate, and heavy precipitation types. But for the light precipitation, the R_1/R_0 phase maximum is down motion right.

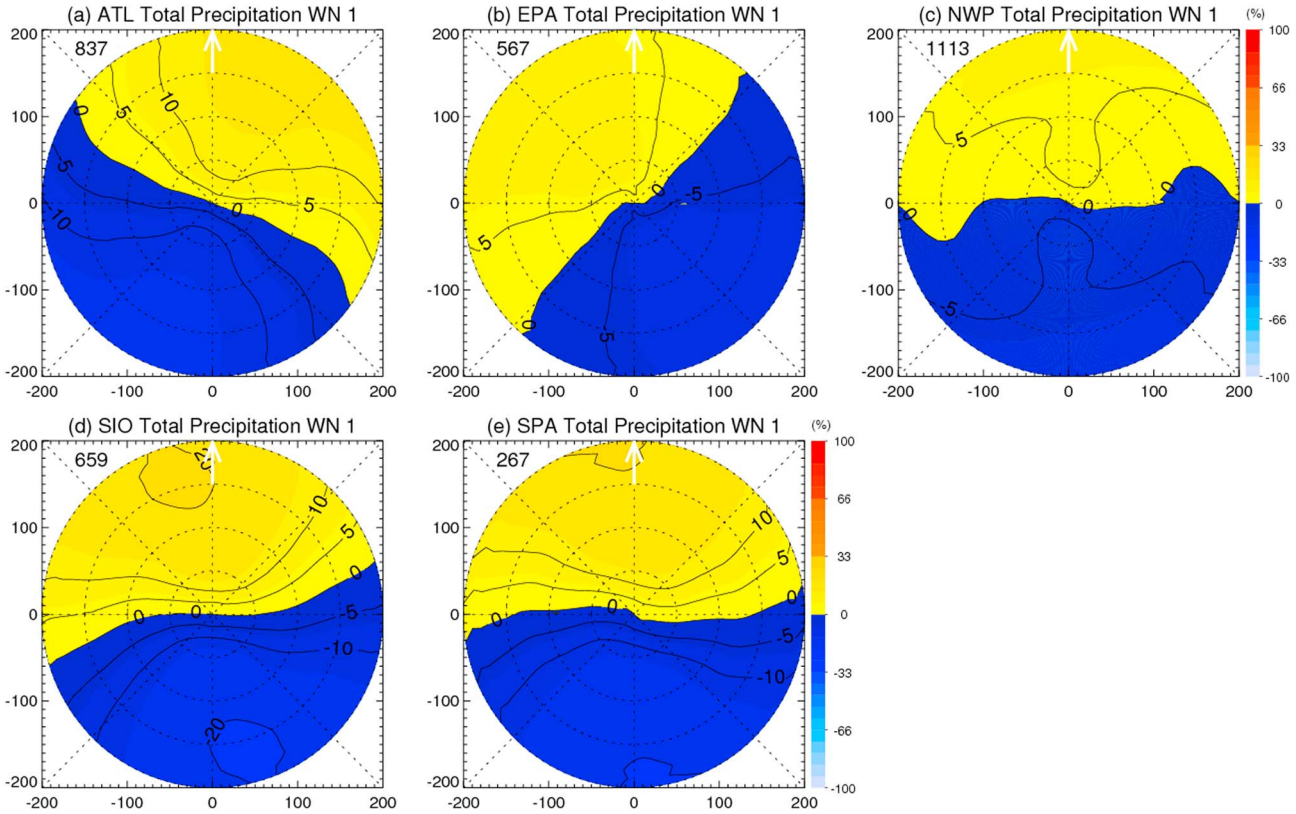

Figure 5. The composite motion-relative wavenumber 1 asymmetry normalized by the azimuthal mean (R_1/R_0, %) of total precipitation for five basins: (a) ATL, (b) EPA, (c) NWP, (d) SIO, and (e) SPA. The white arrow (pointing upward) represents the orientation of motion vector. The color scale represents the amplitude of the normalized wavenumber 1 asymmetry. Dotted range rings represent the 50-, 100-, 150-, and 200-km radii. Overpasses in SIO and SPA are not mirrored. The contours delineate the normalized asymmetry of −20%, −10%, −5%, 0, 5%, 10%, and 20%.

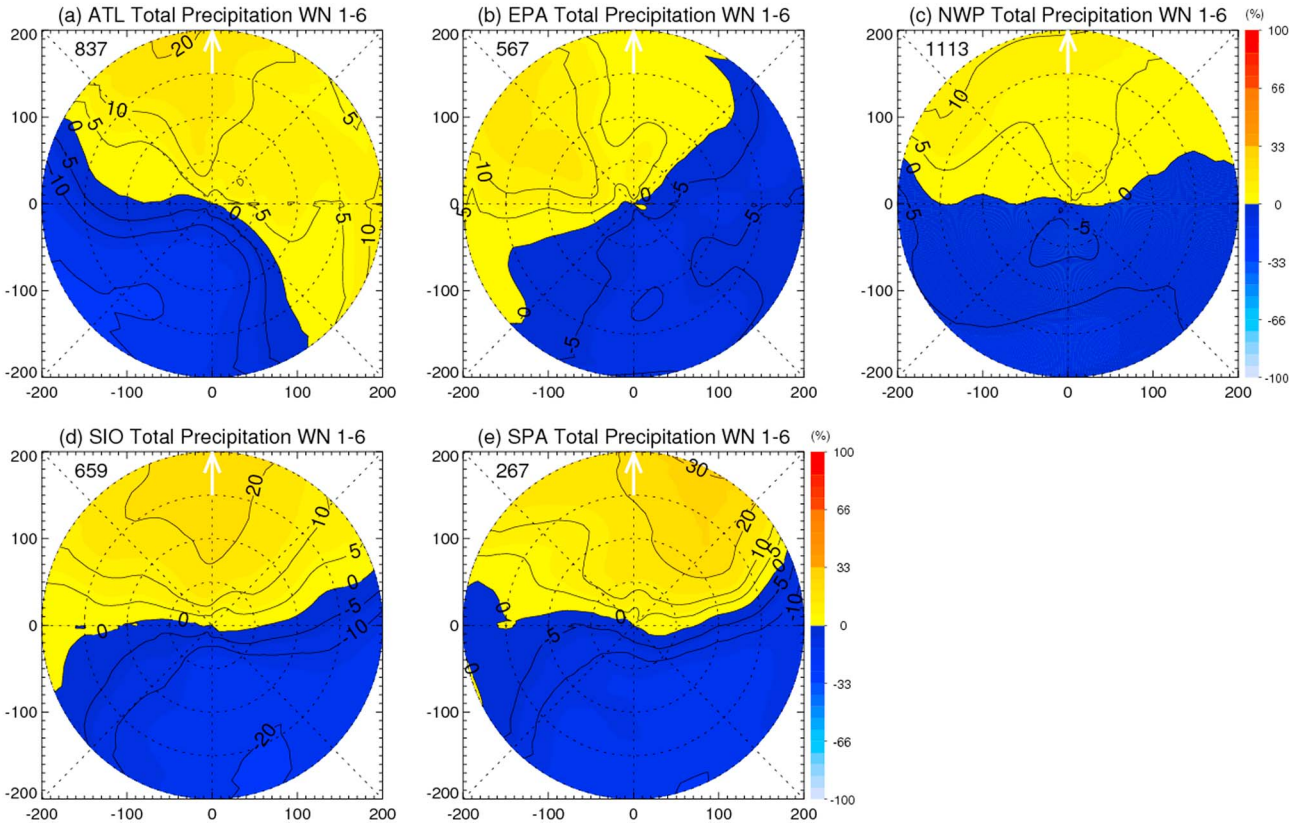

Figure 6. Same as Figure 5 but for $R_{1\text{-}6}/R_0$. The contours in delineate the normalized asymmetry of −20%, −10%, −5%, 0, 5%, 10%, 20%, and 30%.

In LMC04, the rainfall asymmetry is represented by the wavenumber 1 perturbation normalized by the azimuthal mean rain rate, which is R_1/R_0 of total precipitation as shown here in Figure 4IIa. LMC04's Figure 17a shows that the maximum of the normalized wavenumber 1 rainfall asymmetry (R_1/R_0) is down motion in the *outer region*, which is consistent with Figure 4IIa here. However, without the normalization, our results in Figure 4Ia clearly show that the maximum of R_1 is located down motion in the *inner core region*. This difference is caused by the radial variation of the azimuthal mean rain rates (wavenumber 0). As seen in Figure 3, as the radial distance increases from the storm center, the azimuthal mean decreases from 3 to 13 mm/hr in the eyewall region to about 1–3 mm/hr in the 200-km radius region.

After adding the rainfall asymmetry components from wavenumbers 2 to 6 (Figure 4III), the phase maximum of $R_{1\text{-}6}$ stays the same as that of R_1 for light and moderate precipitation types (Figures 4Ib and 4Ic and Figures 4IIIb and 4IIIc). However, the phase maximum of $R_{1\text{-}6}$ turns more toward down motion left than that of R_1 for total and heavy precipitation types (Figures 4Ia and 4Id and Figures 4IIIa and 4IIId). The phase maxima of normalized wavenumber 1–6 asymmetry ($R_{1\text{-}6}/R_0$, Figure 4IV) are all shifted cyclonically to down motion left relative to their wavenumber 1 counterparts (Figure 4II) for all four types of precipitation.

To quantify the amplitude of the wavenumber-based asymmetry, a wavenumber-based asymmetry index for R_1, $R_{1\text{-}6}$, R_1/R_0, or $R_{1\text{-}6}/R_0$ is defined as the mean of all positive values of each of these rainfall asymmetry parameters in each TC overpass. A larger value of the asymmetry index signifies a higher degree of asymmetry. Alvey et al. (2015) and Tao et al. (2017) defined an asymmetry index through a summation of four relevant absolute quadrant differences of polarized corrected brightness temperature or rainfall frequency in the shear-relative coordinate. Our wavenumber-based definition here is different from theirs. Since the Fourier decomposed perturbations explicitly represent the precipitation asymmetry, there is no need to calculate the degree of rainfall asymmetry through quadrant differences.

Table 4
The Asymmetry Index (AI) of the Composite Motion-Relative Wavenumber 1 and Wavenumber 1–6 Asymmetry Normalized by the Azimuthal Mean (R_1/R_0 and $R_{1\text{-}6}/R_0$) of Total Precipitation for Five Basins (Corresponding to Figures 5 and 6)

AI	ATL	EPA	NWP	SIO	SPA
R_1/R_0 (%)	8.5	5.5[c]	4.3[a]	10.8	10.3[b]
$R_{1\text{-}6}/R_0$ (%)	7.6 (−10.6%)	6.2 (12.8%)[c]	4.8 (11.6%)[a]	10.8 (0%)[b]	11.4 (10.7%)[a]

Note. The percentage in each pair of parentheses represents the percentage increase of asymmetry index from R_1/R_0 to $R_{1\text{-}6}/R_0$.
[a]The statistical significance of the value from the value in column ATL at the 99.9% confidence level. [b]The statistical significance of the value from the value in column ATL at the 99% confidence level. [c]The statistical significance of the value from the value in column ATL at the 95% confidence level.

Table 3 shows the wavenumber-based asymmetry indices of composites of R_1, $R_{1\text{-}6}$, R_1/R_0, or $R_{1\text{-}6}/R_0$ corresponding to Figure 4. From Table 3, we can see that the wavenumber-based asymmetry index of R_1 is 0.21 mm/hr for the total precipitation and 0.16 mm/hr for the heavy precipitation, but less than 0.1 mm/hr for both of the light and moderate precipitation. This implies that most of the total precipitation asymmetry is from the heavy precipitation. The contributions for light and moderate precipitation types are small. After adding wavenumber 2–6 components, the wavenumber-based asymmetry index of $R_{1\text{-}6}$ increases by 4.8% and 11.8% from that of R_1 for total and heavy precipitation types, respectively, and no increase is seen for the light and moderate precipitation. This result is consistent with Wingo and Cecil (2010), who found that the majority of the asymmetry in the mean rain rates was accounted for by the asymmetry in the occurrence of heavy rain. After normalized by the azimuthal mean rain rate, the asymmetry index of R_1/R_0 are still similar for the total and heavy precipitation types (second row of Table 3). However, the asymmetry index of $R_{1\text{-}6}/R_0$ increases by 1.7% and 10.9% for the moderate and heavy precipitation, respectively, but decreases by 2.9% for the light precipitation, and no change for the total precipitation, relative to that of R_1/R_0. Statistical significant levels derived from Student's t tests indicate that the mean asymmetry indices of R_1, $R_{1\text{-}6}$, R_1/R_0, and $R_{1\text{-}6}/R_0$ for light, moderate, and heavy precipitation are all significantly different than those of total precipitation, respectively, at the confidence level of 99.9% (Table 3). Student's t tests were also performed for asymmetry indices of $R_{1\text{-}6}/R_0$ and $R_{1\text{-}6}$ relative to those of R_1/R_0 and R_1, respectively (not shown). The result indicates that mean asymmetry indices of $R_{1\text{-}6}/R_0$ and $R_{1\text{-}6}$ are significantly higher than those of R_1/R_0 and R_1, respectively, at the confidence level of 99.9%, respectively. Significant tests have been done for all of the 2-D figures shown in the following tests. Most of them are statistically significant at 95% confidence level or above, with the rest at 90% confidence level. The significant level for each figure is indicated in its corresponding table. For example, the corresponding table of Figures 5 and 6 is Table 4 as labeled in Table 4's title.

For simplicity and a direct comparison with results in LMC04 and CKM06, we will only present the normalized wavenumber 1 and 1–6 asymmetry parameters (R_1/R_0 and $R_{1\text{-}6}/R_0$) for the total precipitation in the following text. Figure 5 presents the composite of the motion-relative wavenumber 1 asymmetry normalized by the azimuthal mean (R_1/R_0) of total precipitation over five different oceanic basins (note that SH overpasses are not mirrored in this figure). Note that results from the NIO basin are not shown in Figures 5, 6, 9, and 10 due to small sample size and statistical insignificance of these results. The location of maximum R_1/R_0 of total precipitation is mainly down motion, especially in the NWP and SPA basins (Figures 5c and 5f). This is consistent with earlier observational studies showing that the rainfall maximum in the inner core region is mainly located at down motion quadrants (Burpee & Black, 1989; Marks, 1985; Miller, 1958; Reasor et al., 2000; Willoughby et al., 1984) and theoretical modeling studies showing that the boundary layer convergence and upward motion are in down motion quadrants as well (Frank & Ritchie, 1999; Shapiro, 1983). In ATL (Figure 5a), there is a right of motion component; while in EPA (Figure 5b) and SIO (Figure 5d), there is a left of motion component. The results in Figure 5 for each basin are generally consistent with the results shown in LMC04's Figure 18 for the radius of within 0–200 km. The ATL result of down motion right preference is also similar to Corbosiero and Molinari (2003), which showed a down motion right maximum of lightning distributions in ATL hurricanes.

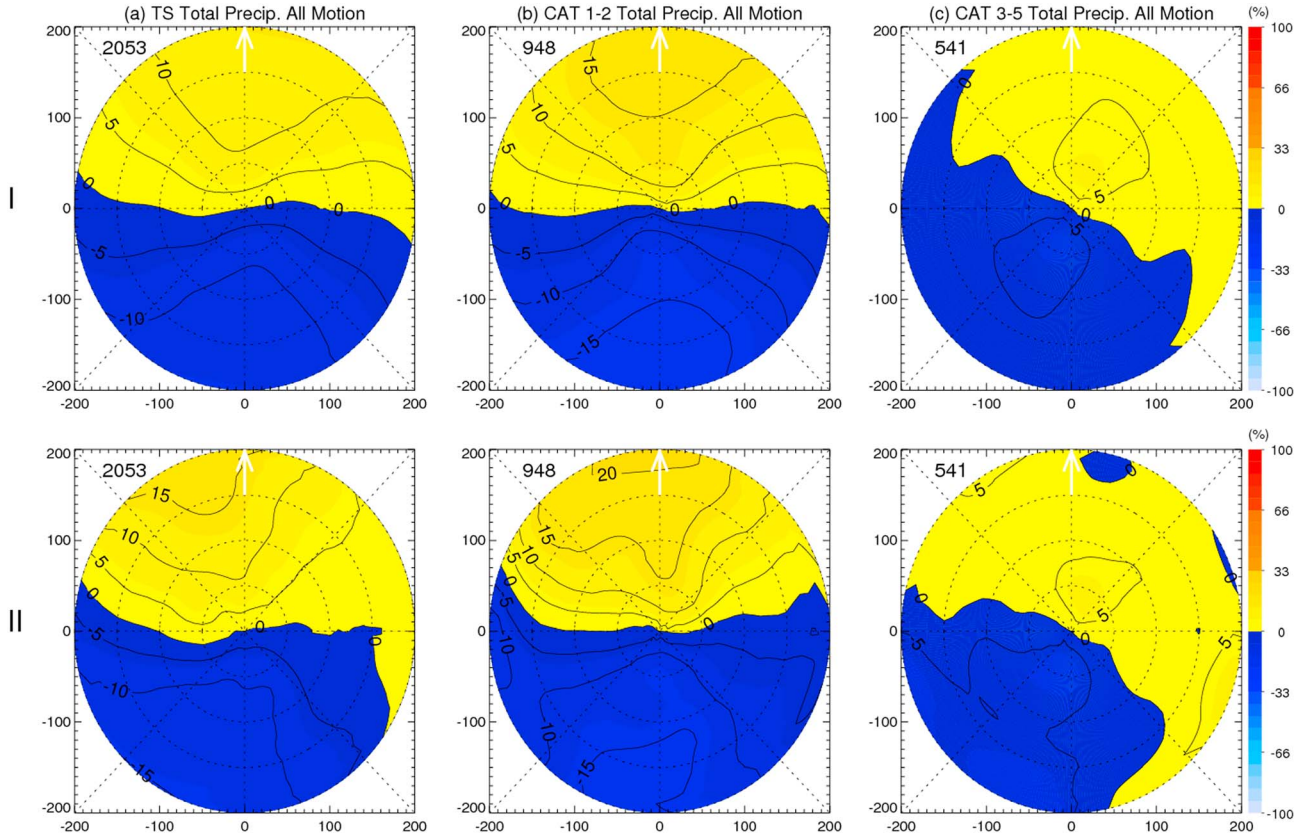

Figure 7. The composite motion-relative R_1/R_0 (%) in row I and $R_{1\text{-}6}/R_0$ (%) in Row II of total precipitation for different tropical cyclone intensity groups: (a) tropical storm (TS), (b) CAT1-2, and (c) CAT3-5. The white arrow (pointing upward) represents the orientation of motion vector. The color scale represents the amplitude of the normalized wavenumber 1 asymmetry. Dotted range rings represent the 50-, 100-, 150-, and 200-km radii. The contours delineate the normalized asymmetry of −15%, −10%, −5%, 0, 5%, 10%, and 15%.

Figure 6 presents the composite motion-relative wavenumber 1–6 asymmetry normalized by the azimuthal mean ($R_{1\text{-}6}/R_0$) of total precipitation over five oceanic basins. Compared with the normalized wavenumber 1 asymmetry shown in Figure 5, the amplitude of the motion-relative wavenumber 1–6 asymmetry is higher. It is also interesting to note that, by adding wavenumbers 2–6 to wavenumber 1, the phase maximum of wavenumber 1–6 asymmetry shifts cyclonically around the TC center in all the basins. For example, the phase maximum of ATL and NWP TCs shifts from down motion or down motion right to down motion left, while that of SH TCs shifts from down motion left to down motion or down motion right.

Table 5
The Asymmetry Index (AI) of the Composite Motion-Relative R_1/R_0 and $R_{1\text{-}6}/R_0$ of Total Precipitation for Different TC Intensity Groups: TS, CAT1-2, and CAT3-5 (Corresponding to Figure 7)

AI	TS	CAT1-2	CAT3-5
R_1/R_0 (%)	6.8	9.2[a]	3.6[a]
$R_{1\text{-}6}/R_0$ (%)	6.6 (−2.9%)	10.1 (9.8%)[a]	3.5 (−2.7%)[a]

Note. The percentage in each pair of parentheses represents the percentage increase of asymmetry index from R_1/R_0 to $R_{1\text{-}6}/R_0$.
[a]The statistical significance of the value from the value in the previous column at the 99.9% confidence level.

From Table 4, we can see that SH TCs have the highest motion-relative asymmetry indices of R_1/R_0 and $R_{1\text{-}6}/R_0$, followed by ATL, EPA, and NWP TCs in decreasing order. This indicates that rainfall asymmetry of TCs in the SH basins has more variability that can be explained by the motion effect. By adding wavenumbers 2–6, the increase of the asymmetry index is highest for EPA (12.8%) and is lowest for ATL (−10.6%). It indicates that EPA (ATL) TCs have more (less) rainfall asymmetry contributed by higher wavenumbers than TCs in the other basins.

Figure 7 shows the motion-relative composite of R_1/R_0 (Figure 7I) and $R_{1\text{-}6}/R_0$ (Figure 7II) for each intensity group. The phase maximum of R_1/R_0 for both the TS (Figure 7Ia) and CAT1-2 (Figure 7Ib) TCs is down motion, while that for CAT3-5 TCs (Figure 7Ic) is located down motion right. In general, the effect of motion due to friction-induced convergence causes the

Table 6
The Asymmetry Index (AI) of the Composite Motion-Relative R_1/R_0 and $R_{1\text{-}6}/R_0$ of Total Precipitation for TS Under Slow Motion and Fast Motion (Corresponding to Figure 8)

TS	AI of R_1/R_0 (%)	AI of $R_{1\text{-}6}/R_0$ (%)
Slow Motion	5.0	4.7 (−6.0%)
Fast Motion	9.6[d]	10.4 (8.3%)[b]

Note. The percentage in each pair of parentheses represents the percentage increase of asymmetry index from R_1/R_0 to $R_{1\text{-}6}/R_0$.
[b]The statistical significance of the value from the value in the previous row at the 99% confidence level only between slow and fast motion categories. [d]The statistical significance of the value from the value in the previous row at the 90% confidence level only between slow and fast motion categories.

asymmetry maximum to be located down motion. As storm intensity increases, stronger tangential winds will cause the asymmetry maximum to shift to the right of motion, as we see in Figure 7lc for major hurricanes. This is generally consistent with LMC04's results in their Figure 17.

However, in terms of the asymmetry amplitude, LMC04 found that the amplitude decreases as the TC intensity increases. This is different from what we found here. As shown in Table 5, the asymmetry index of R_1/R_0 is the highest for CAT1-2, which is higher than that of TS and CAT3-5 TCs. The general understanding is that as the storm intensity increases, the primary circulation should be stronger and more symmetric because the shear magnitude decreases with increasing storm intensity (Table 2; Marks & Houze 1987) and the stronger vortex is more resilient to shear and motion effects (Reasor et al., 2013; Reasor & Eastin, 2012). Our result here shows that the precipitation of major hurricanes is the most symmetric relative to motion, but that of Category 1 and 2 hurricanes is more asymmetric than that of tropical storms. This essentially indicates that more variability in the spatial distribution of rainfall of CAT1-2 hurricanes

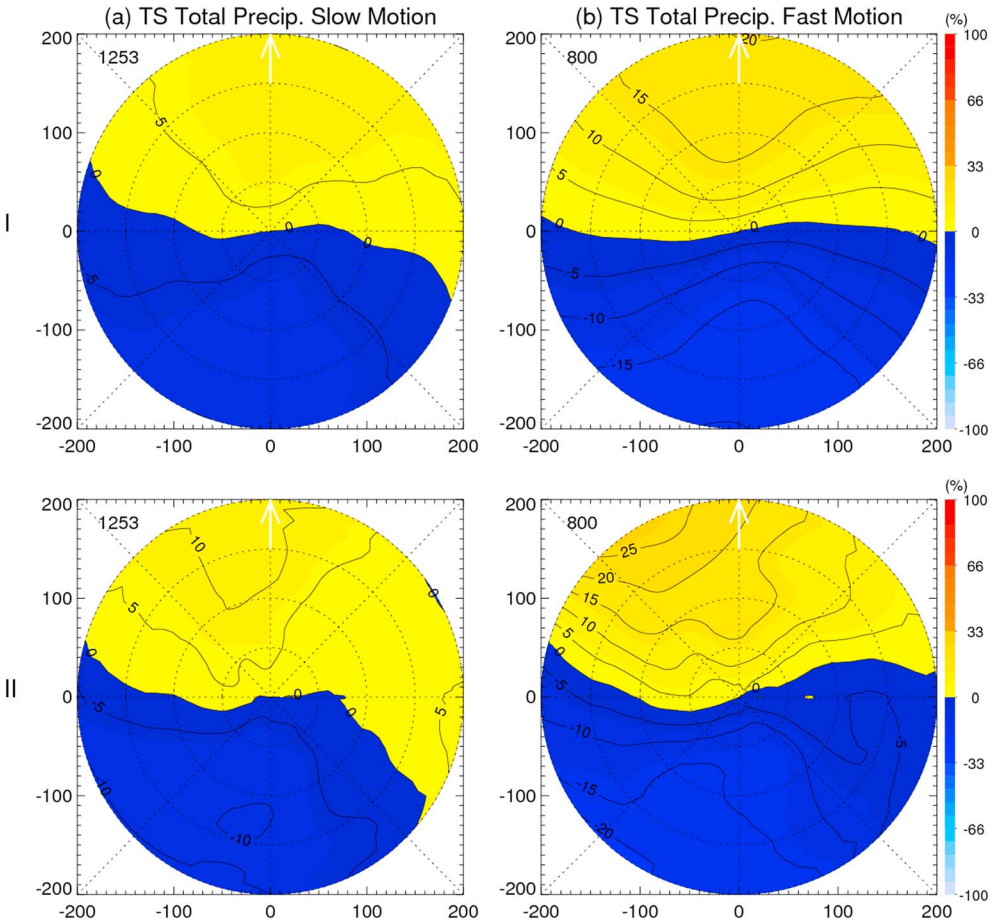

Figure 8. The composite motion-relative R_1/R_0 (%) in Row I and $R_{1\text{-}6}/R_0$ (%) in Row II of total precipitation for different tropical storms (TSs) under a slow motion and b fast motion speeds. The white arrow (pointing upward) represents the orientation of motion vector. The color scale represents the amplitude of the normalized wavenumber 1 asymmetry. Dotted range rings represent the 50-, 100-, 150-, and 200-km radii. The contours delineate the normalized asymmetry of −20%, −10%, −5%, 0, 5%, 10%, 15%, 20%, and 25%.

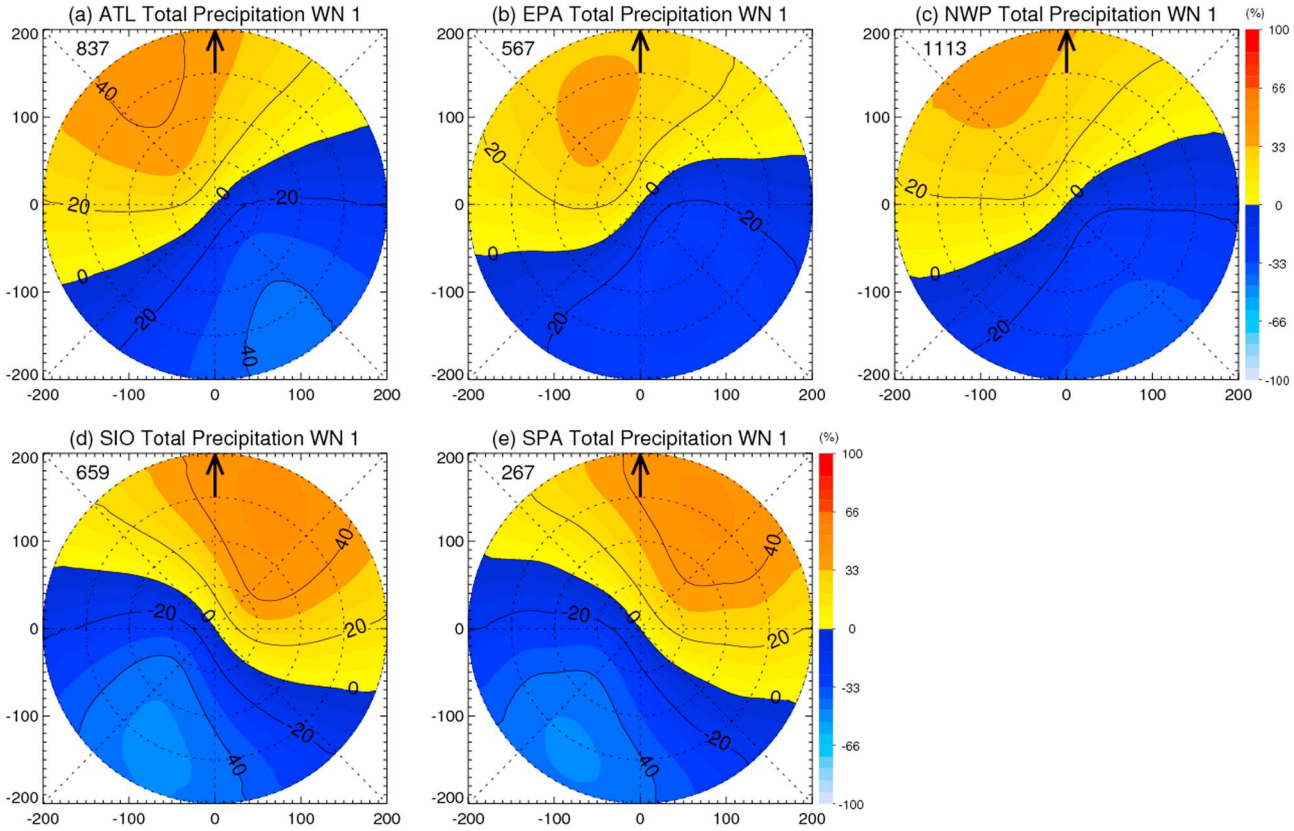

Figure 9. The composite shear-relative wavenumber 1 asymmetry normalized by the azimuthal mean (R_1/R_0, %) of total precipitation for five basins: (a) ATL, (b) EPA, (c) NWP, (d) SIO, and (e) SPA. The black arrow (pointing upward) represents the orientation of shear vector. The color scale represents the amplitude of the normalized wavenumber 1 asymmetry. Dotted range rings represent the 50-, 100-, 150-, and 200-km radii. Overpasses in SIO and SPA are not mirrored. The contours delineate the normalized asymmetry of −40%, −20%, 0, 20%, and 40%.

may be explained by the motion relative system than that of tropical storms. Similarly, Klotz and Jiang (2016) found that the motion effects impact the surface wind speed asymmetry of CAT1-2 hurricanes more strongly than that of TSs. They hypothesized that "Categories 1 and 2 hurricanes represents a transition threshold between which motion and shear impacts are both influencing the vortex in similar capabilities." The motion effect is through the surface friction induced by the storm motion. As shown by previous studies (Powell, 1980; Powell et al., 2003), friction velocities in TCs increase with increasing wind speed up to about 40 m/s, after which they begin to decrease slightly. This supports the hypothesis that the asymmetry of vortex and rainfall field of Categories 1 and 2 hurricanes is more affected by motion factors than that of storms either weaker or stronger than the CAT1-2 intensity.

Table 7
The Asymmetry Index (AI) of the Composite Shear-Relative Wavenumber 1 and Wavenumber 1–6 Asymmetry Normalized by the Azimuthal Mean (R_1/R_0 and $R_{1\text{-}6}/R_0$) of Total Precipitation for Five Basins (Corresponding to Figures 9 and 10)

AI	ATL	EPA	NWP	SIO	SPA
R_1/R_0 (%)	21.9	19.5[c]	18.4[a]	25.5	24.1[b]
$R_{1\text{-}6}/R_0$ (%)	25.8 (17.8%)	24.9 (27.7%)[c]	21.6 (17.4%)[a]	30.8 (20.8%)[b]	27.9 (15.8%)[a]

Note. The percentage in each pair of parentheses represents the percentage increase of asymmetry index from R_1/R_0 to $R_{1\text{-}6}/R_0$.
[a]The statistical significance of the value from the value in column ATL at the 99.9% confidence level. [b]The statistical significance of the value from the value in column ATL at the 99% confidence level. [c]The statistical significance of the value from the value in column ATL at the 95% confidence level.

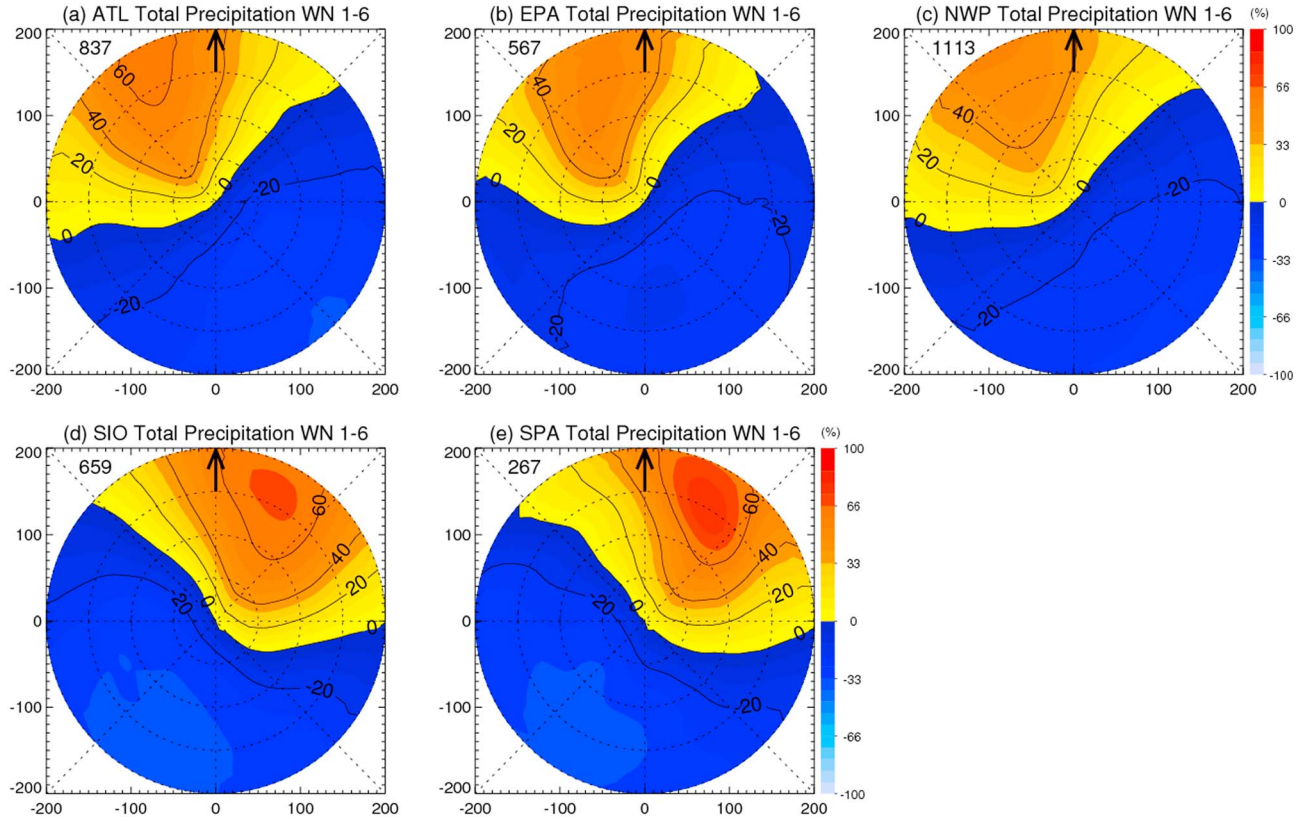

Figure 10. Same as Figure 9 but for $R_{1\text{-}6}/R_0$. The contours delineate the normalized asymmetry of −20%, 0, 10%, 20%, 40%, and 60%.

After adding the asymmetry components of higher wavenumbers (wavenumbers 2–6), the phase maximum in each panel of Figure 7II shifts cyclonically around the storm center relative to the corresponding panel of Figure 7I. This cyclonic shift is similar as what we found from Figures 5 to 6. After dividing the samples in each intensity group into slow (<5 m/s) and fast (>5 m/s) motion speeds, Student *t* tests show that differences between fast-motion and slow-motion cases are statistically significant for TSs (Table 6), but not for CAT1-2 and CAT3-5 hurricanes. Figure 8 shows the motion-relative composite of R_1/R_0 (Figure 8I) and $R_{1\text{-}6}/R_0$ (Figure 8II) for fast-motion and slow-motion TSs. By adding the asymmetry components of wavenumbers 2–6, the cyclonic shift of phase maxima persists when dividing TS samples into slow and fast-moving cases. The phase maximum remains unchanged from slow-motion to fast-motion TSs (Figure 8). We can see from Table 6 that both of the wavenumber 1 and wavenumber 1–6 asymmetry amplitudes are significantly higher for fast than slow motion TS cases.

3.4. Shear Effect

Figure 9 presents the composite shear-relative R_1/R_0 of total precipitation over five oceanic basins. The phase maximum of the normalized wavenumber 1 asymmetry (R_1/R_0) is clearly downshear left in the NH and downshear right in the SH basins. This is consistent with many previous studies (e.g., Corbosiero & Molinari, 2002; CKM06; Cecil, 2007; Ueno, 2007; Wingo & Cecil, 2010). Comparing Table 4 with Table 7, the asymmetry index of R_1/R_0 for storms in each basin relative to the vertical wind shear is more than twice as large as that relative to the storm motion. In agreement with CKM06, our results strongly suggest that the vertical wind shear is a more important factor in producing the precipitation asymmetry.

The composite shear-relative $R_{1\text{-}6}/R_0$ of total precipitation over five oceanic basins is shown in Figure 10. After adding higher wavenumber components, the phase maximum in each panel of Figure 10 does not change from that in Figure 9. The amplitude of the asymmetry increases after adding wavenumber 2–6

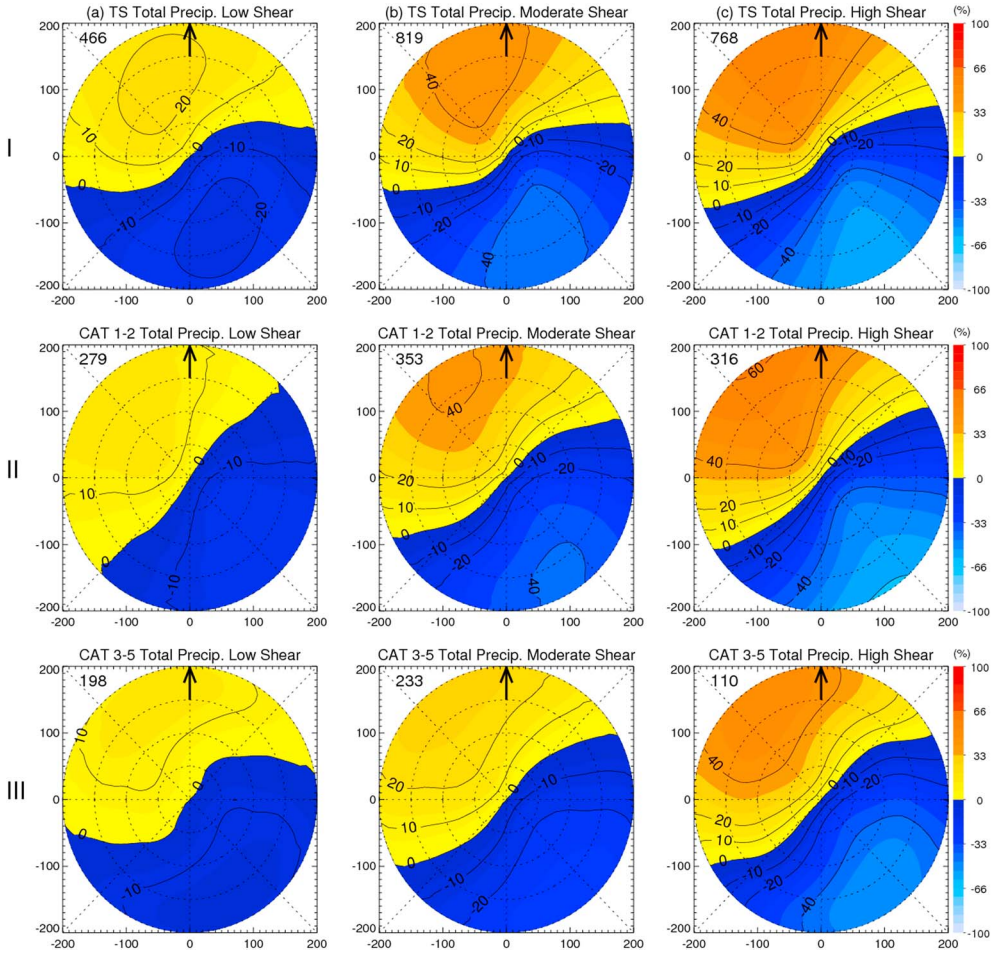

Figure 11. The composite shear-relative R_1/R_0 (%) of total precipitation for different tropical cyclone intensity groups: (I) tropical storm (TS), (II) CAT1-2, and (III) CAT3-5 under various environmental wind shear magnitudes: (a) low shear, (b) moderate shear, and (c) high shear. The black arrow (pointing upward) represents the orientation of shear vector. The color scale represents the amplitude of the normalized wavenumber 1 asymmetry. Dotted range rings represent the 50-, 100-, 150-, and 200-km radii. The contours delineate the normalized asymmetry of −40%, −20%, −10%, −0, 10%, 20%, 40%, and 60%.

components. As seen in Table 7, the asymmetry index of the shear-relative $R_{1\text{-}6}/R_0$ is about 15% to 30% higher than that of R_1/R_0 for storms in each basin. TCs in the SIO basin have the largest asymmetry indices of R_1/R_0 and $R_{1\text{-}6}/R_0$, while TCs in the NWP basin have the smallest asymmetry indices of R_1/R_0 and $R_{1\text{-}6}/R_0$. Storms in the SPA basin have the smallest percentage increase of asymmetry index from R_1/R_0 to $R_{1\text{-}6}/R_0$. In general, the total precipitation of TCs in SH basins are more asymmetric than that in ATL, EPA, and NWP basins in both the shear-relative (Table 7) and motion-relative (Table 4) frameworks.

Figure 11 demonstrates the shear-relative R_1/R_0 of total precipitation by dividing the samples in each of the three intensity groups into three subsets with shear values <5 (low shear), 5–10 (moderate shear), and >10 (high shear) m/s. Similar to Figure 10, the maximum of the wavenumber 1 asymmetry of total precipitation is generally downshear left for all cases. As the TC intensity increases from TS to CAT1-2, the asymmetry phase maximum shifts slightly cyclonically to the left, similar as CKM06. The phase maximum stays the same as TC intensity increases from CAT1-2 to CAT3-5, especially for the moderate and high shear groups. CKM06 found in their Figure 8 that the maximum of the normalized wavenumber 1 asymmetry (R_1/R_0) was downshear left for TCs in moderate to high shear conditions but was mostly downshear when the shear is <5 m/s. Their findings for the moderate and high shear conditions are the same as we found here in Figures 11b and 11c. But for the low shear condition, we found in this study that the phase maximum is still downshear left

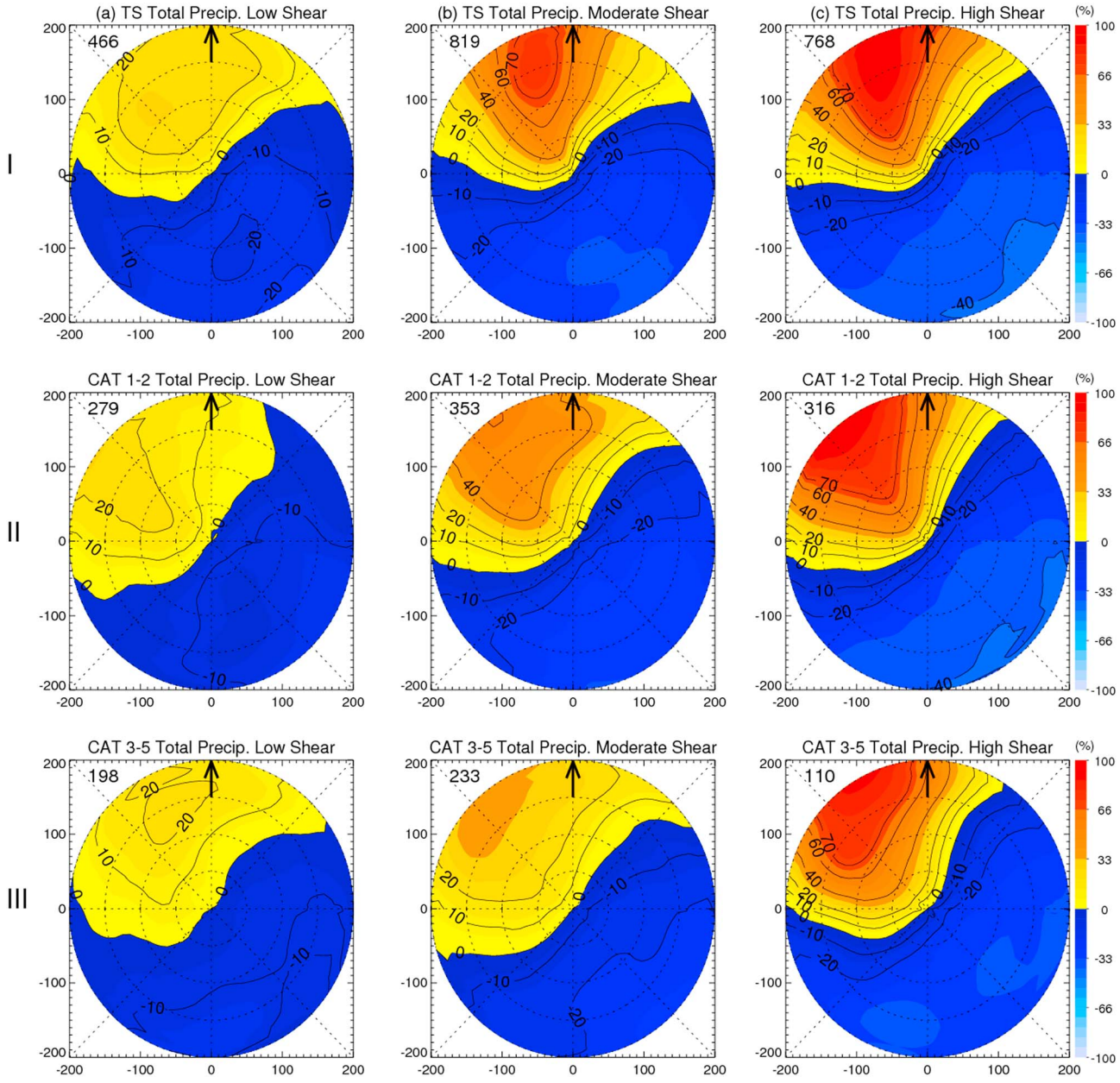

Figure 12. Same as Figure 11 but for $R_{1\text{-}6}/R_0$. The contours delineate the normalized asymmetry of −20%, −10%, −0, 10%, 20%, 40%, 60%, and 70%.

(Figure 11a). CKM06 used the same TMI samples as in LMC04. It is noted that LMC04's sample includes quite a lot overpasses in which the TC was not fully captured by the TMI. In LMC04, the criterion of overpass selection was that at least 20% of the total area within 500-km radius is covered by the TMI. In contrast, we require 100% coverage by the TMI for the area within 200-km radius. The sample selection difference may be the main reason for the difference between our results and CKM06's.

After adding asymmetry components from wavenumbers 2–6, the phase maximum stays unchanged (still downshear left, Figure 12). However, a striking increase in asymmetry amplitude is seen in Figure 12 compared with Figure 11. As shown in Table 8, the percentage increase in the asymmetry index after adding wavenumbers 2–6 ranges from 9 to 30%, with the highest increase occurring in high shear groups. Lonfat et al. (2007) introduced the Parametric Hurricane Rainfall Model (PHRaM), which failed at producing strong

Table 8
The Asymmetry Index (AI) of the Composite Shear-Relative R_1/R_0 and $R_{1\text{-}6}/R_0$ of Total Precipitation for Three Intensity Groups: TS, CAT1-2, and CAT3-5 Under Low, Moderate, and High Environmental Shear Conditions (Corresponding to Figures 11 and 12)

	Low	Moderate	High
AI: R_1/R_0 (%)			
TS	12.5	24.9[a]	29.9[a]
CAT1-2	9.4[a1]	20.9[a, a1]	29.3[a, a1]
CAT3-5	7.6 [a1]	14.5[b, a1]	25.4[a, a1]
AI: $R_{1\text{-}6}/R_0$ (%)			
TS	14.0 (12%)	30.4 (22%)[a]	37.1 (24%)[a]
CAT1-2	10.6 (13%)[a1]	24.4 (17%)[a, a1]	36.7 (25%)[a, a1]
CAT3-5	8.8 (16%)[a1]	15.8 (9%)[a1]	33.0 (30%)[a, a1]

Note. The percentage in each pair of parentheses represents the percentage increase of asymmetry index from R_1/R_0 to $R_{1\text{-}6}/R_0$.
[a]The statistical significance of the value from the value in the previous column at the 99.9% confidence level. [b]The statistical significance of the value from the value in the previous column at the 99% confidence level. [a1]The statistical significance of the value from the value in the previous row at the 99.9% confidence level.

rainfall asymmetries caused by the vertical wind shear. They argued that the failure is possibly because the model was based on the average statistical satellite observation. However, from our results here, the failure is also likely due to only including first- and second-order rainfall asymmetries in PHRaM. Adding higher wavenumber perturbations would possibly provide more accurate precipitation forecasts or simulations. One can use the asymmetry pattern shown in Figure 12 to parameterize the asymmetric rainfall pattern relative to shear direction and magnitude and storm intensity and apply that pattern to a parametric rain model for TC hazard assessment. Also seen in Table 8, asymmetry indices of R_1/R_0 and $R_{1\text{-}6}/R_0$ for the high shear group are a factor of 1.5 higher than those for the moderate shear group, which are twice as high as those for the low shear group. Asymmetry indices of R_1/R_0 and $R_{1\text{-}6}/R_0$ decrease as TC intensity increases for both low, moderate, and high shear conditions. This is different with the results in Figure 6 under the motion-relative framework.

3.5. Motion and Shear Combined Effect

To examine the combined effect of storm motion and vertical wind shear to the TC rainfall asymmetry, the samples are grouped such that the shear vectors are in the same, opposite, right, and left of the TC motion directions. All cases in Figure 13 display a dominant downshear left asymmetry maximum regardless of the shear vector orientation to the TC motion, similar to CKM06. When the shear and motion are in the same direction, or the shear to the right of motion, combination of motion-induced down motion and the shear-induced downshear left components creates a favorable overlap in the downshear left quadrant (Figures 13Ia and 13Ic). When the shear and motion vectors are in the opposite directions, or the shear to the left of the motion, the phase maximum of rainfall asymmetry is only shifted slightly, still downshear left but more toward downshear (Figures 13Ib and 13Id). The

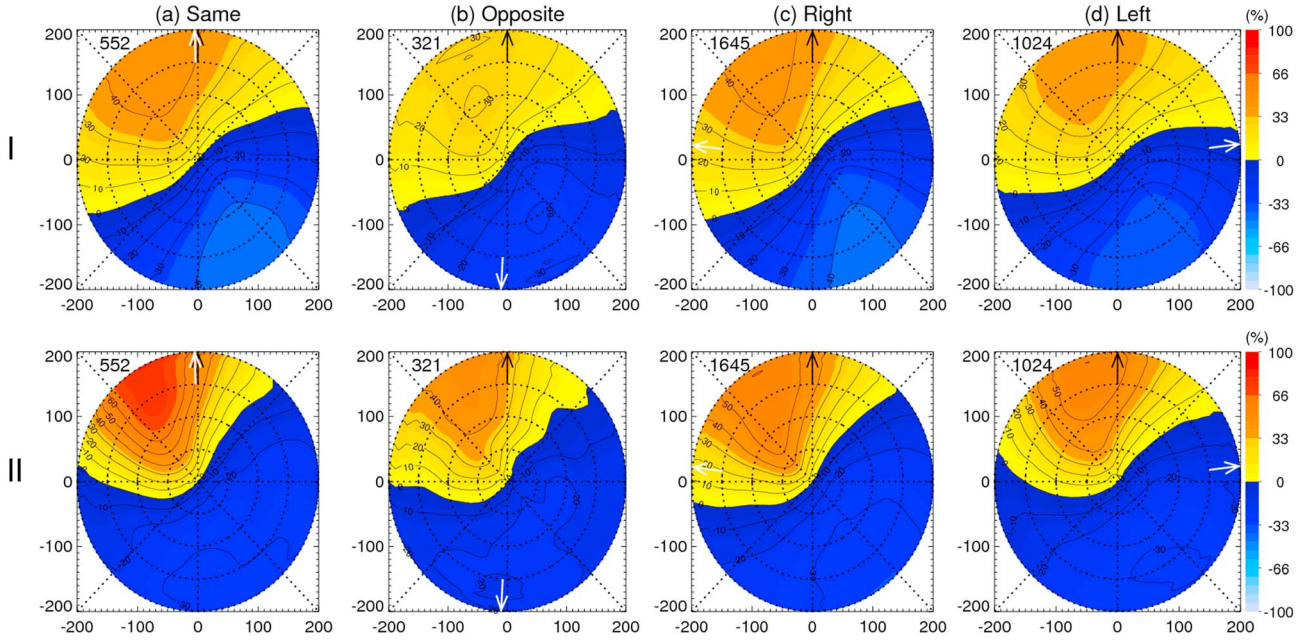

Figure 13. The composite shear-relative (I) R_1/R_0 (%) and (II) $R_{1\text{-}6}/R_0$ (%) of total precipitation with the shear direction (a) same as, (b) opposite to, (c) to the right of, and (d) to the left of the motion direction for the black arrow (pointing upward) represents the orientation of vertical wind shear vector. The white arrow represents the mean orientation of motion vector. The color scale represents the amplitude of the normalized wavenumber 1 asymmetry. Dotted range rings represent the 50-, 100-, 150-, and 200-km radii. The contours delineate the normalized asymmetry of −40%, −30%, −20%, −10%, 0, 10%, 20%, 30%, 40%, and 50%.

Table 9
The Asymmetry Index (AI) of the Composite Shear-Relative (I) R_1/R_0 and (II) $R_{1\text{-}6}/R_0$ of Total Precipitation With the Shear Direction (a) Same as, (b) Opposite to, (c) to the Right of, and (d) to the Left of the Motion Direction (Corresponding to Figure 13)

AI	(a) Same	(b) Opposite	(c) Right	(d) Left
I. R_1/R_0 (%)	23.2	16.6	22.7[d]	20.2
II. $R_{1\text{-}6}/R_0$ (%)	30.0 (29%)	20.3 (22%)[c]	26.7 (18%)[b]	24.0 (19%)[d]

Note. The percentage in each pair of parentheses represents the percentage increase of asymmetry index from R_1/R_0 to $R_{1\text{-}6}/R_0$.
[b]The statistical significance of the value from the value in column (a) at the 99% confidence level. [c]The statistical significance of the value from the value in column (a) at the 95% confidence level. [d]The statistical significance of the value from the value in column (a) at the 90% confidence level.

asymmetry amplitude is the largest when the shear and motion vectors are in the same directions and the smallest when they are opposite (Table 9). This is consistent with CKM06 who found that the wavenumber 1 rainfall asymmetry maximum is downshear left in the inner-core region (within 150-km radius of the TC center) for both low shear and high shear conditions and varies only slightly with the TC motion vector relative to the shear vector. Both of our results and CKM06's indicate that the shear effect is dominant over the motion effect for determining the wavenumber 1 rainfall asymmetry. After adding wavenumber 2–6 components, above features stay the same, expect that the amplitude of asymmetry increases by about 18–30% (Figure 13II and Table 9).

Furthermore, the samples of the four groups (same, opposite, right, and left) are subdivided by the strength of the shear value and the motion speed. This is similar to CKM06, but they only had eight subgroups including strong shear and weak shear conditions for each of the four shear-motion orientation groups. The larger sample size used in this study allows us to further stratify each of the four shear-motion orientation groups into six subsets including slow motion and low shear, slow motion and moderate shear, slow motion and

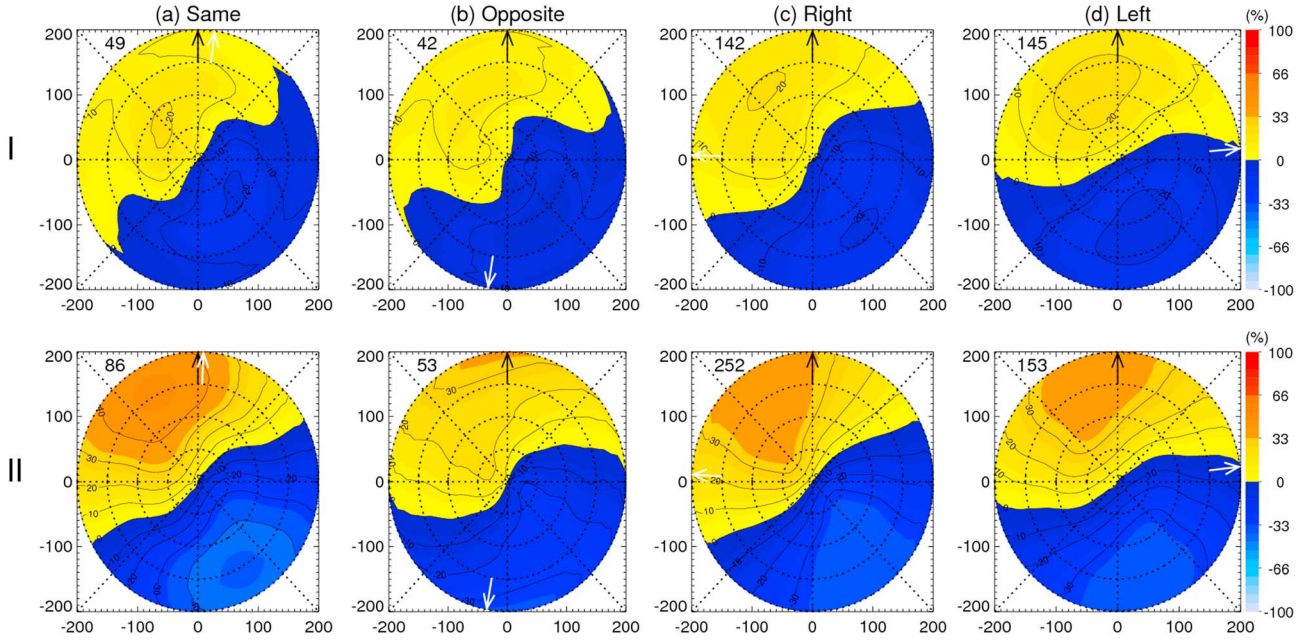

Figure 14. The composite shear-relative R_1/R_0 of total precipitation with the shear direction (a) same as, (b) opposite to, (c) to the right of, and (d) to the left of the motion direction for (I) fast motion and low shear and (II) fast motion and moderate shear conditions. The black arrow (pointing upward) represents the orientation of vertical wind shear vector. The white arrow represents the mean orientation of motion vector. The color scale represents the amplitude of the normalized wavenumber 1 asymmetry. Dotted range rings represent the 50-, 100-, 150-, and 200-km radii. The contours delineate the normalized asymmetry of −40%, −30%, −20%, −10%, 0, 10%, 20%, 30%, and 40%.

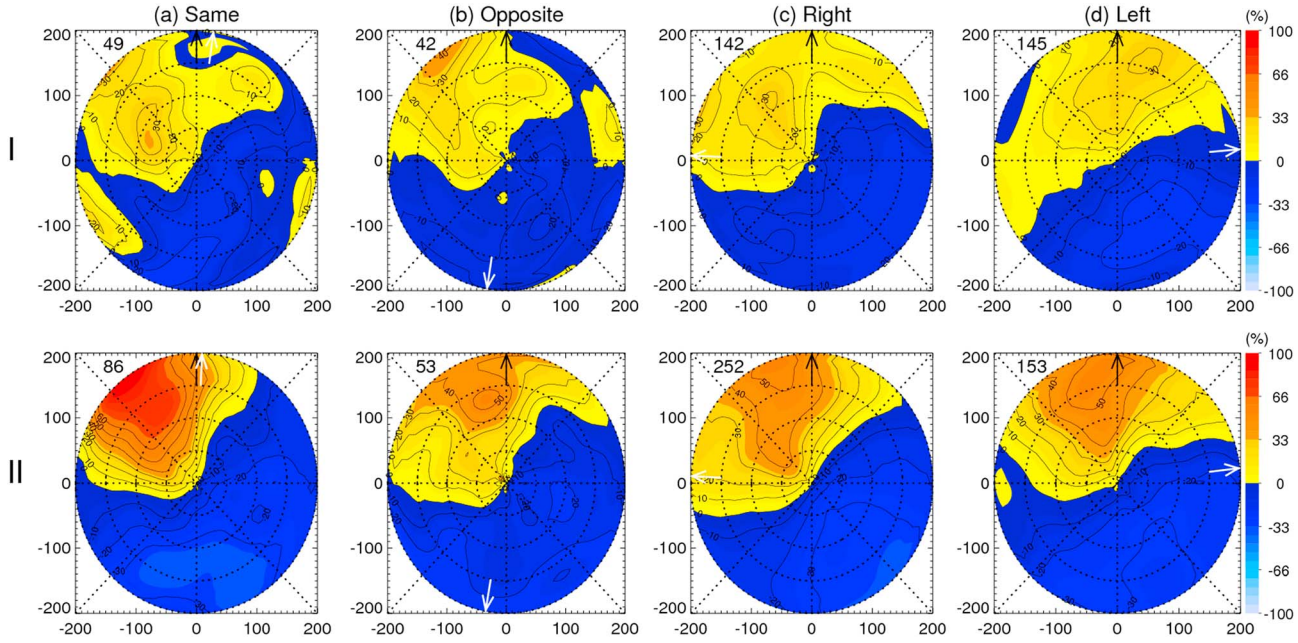

Figure 15. Same as Figure 14 but for the composite shear-relative $R_{1\text{-}6}/R_0$ of total precipitation. The contours delineate the normalized asymmetry of −30%, −20%, −10%, 0, 10%, 20%, 30%, 40%, 50%, and 60%.

high shear, fast motion and low shear, fast motion and moderate shear, and fast motion and high shear conditions. The composites shear-relative R_1/R_0 and $R_{1\text{-}6}/R_0$ of total precipitation for the 24 subgroups were plotted but only the subgroups of fast motion and low shear (Figures 14I and 15I) and fast motion moderate shear (Figures 14II and 15II) are shown due to statistically insignificant results of other subgroups. The most striking feature is that all cases of the 24 subgroups display a dominant downshear-left asymmetry maximum regardless of the shear vector orientation to the TC motion, the magnitude of the shear value, and the speed of TC motion, consistent with Figure 13. After adding wavenumber 2–6 components, the maximum asymmetry of $R_{1\text{-}6}/R_0$ is still downshear left for all subgroups except for the group with low shear, fast motion, and the shear vector left to the motion (Figure 15Id), in which case the phase maximum is downshear right. This implies that when the shear is low and the motion speed is fast, the motion-induced down motion left component of wavenumbers 1–6 (see Figure 6) becomes a more important factor. For the subgroups with fast motion low shear and when the shear and motion vectors are in the opposite directions (Figure 15b), or when the shear to the left of the motion (Figure 15d), the motion-induced down motion left component makes the downshear left preference shifted slightly toward downshear. The asymmetry index increases 2–32% for all cases shown in Figures 13 and 14 after adding higher wavenumber components (Table 10).

Table 10
The Asymmetry Index (AI) of the Composite Shear-Relative R_1/R_0 and $R_{1\text{-}6}/R_0$ of Total Precipitation With the Shear Direction (a) Same as, (b) Opposite to, (c) to the Right of, and (d) to the Left of the Motion Direction (I) Fast Motion and Low Shear, (II) Fast Motion and Moderate Shear (Corresponding to Figures 14 and 14)

	(a) Same	(b) Opposite	(c) Right	(d) Left
AI: R_1/R_0 (%)				
I	9.8	8.0	10.7[c]	11.6[c]
II	23.6	15.9[d]	21.7	19.4
AI: $R_{1\text{-}6}/R_0$ (%)				
I	12.1 (23%)	10.3 (29%)	12.9 (21%)[b]	11.8 (2%)[c]
II	31.2 (32%)	19.6 (23%)	24.3 (12%)	22.4 (15%)[d]

Note. The percentage in each pair of parentheses represents the percentage increase of asymmetry index from R_1/R_0 to $R_{1\text{-}6}/R_0$.
[b]The statistical significance of the value from the value in column (a) at the 99% confidence level. [c]The statistical significance of the value from the value in column (a) at the 95% confidence level. [d]The statistical significance of the value from the value in column (a) at the 90% confidence level.

The results above in Figures 13 and 14 and Table 10 are for the composite in the shear-relative framework. To test if the results still hold in the motion-relative framework, we have plotted the composites motion-relative R_1/R_0 and $R_{1\text{-}6}/R_0$ of total precipitation for all the 24 subgroups (not shown). When composited relative to the motion vector, the maximum asymmetry is down motion left, up motion right, down motion right, and left of motion when the shear vector is in the same, opposite, right, and left of the TC motion directions, respectively. Using the average shear direction in each motion-relative composite, it is found that all the cases display a down shear left maximum, except that the wavenumber 1–6

asymmetry is down shear right when the shear magnitude is low and the shear vector is left of the TC motion vector. This is consistent with the shear relative results in Figures 14 and 15 and confirms that the shear effect is dominant over the motion.

4. Conclusions

Sixteen years (1998–2013) of TRMM TMI-retrieved rain rate data are employed to quantify low and higher wavenumber asymmetries of four types of precipitation using the Fourier wavenumber decomposition method. The energy spectrum of rainfall perturbation and impacts of the storm motion and environmental vertical shear to the rainfall asymmetry are analyzed. It is found that although the wavenumber 1 perturbation is the largest in the energy spectrum, it only contributes 37% of the total perturbation energy of total precipitation. It is necessary to analyze higher wavenumbers in order to have a better understanding on rainfall asymmetries. In this study, we choose to examine both the wavenumber 1 and the sum of wavenumber 1–6 rainfall perturbations. A little over 70% of the total perturbation energy of total precipitation is from wavenumbers 1 to 6.

In the motion-relative framework, by comparing unnormalized wavenumber 1 and wavenumber 1–6 asymmetry distributions for four types of precipitation, it is found that most of the total precipitation asymmetry is from the heavy precipitation, and contributions for light and moderate precipitation types are small (Figure 4 and Table 3). This is consistent with Wingo and Cecil's (2010) results. The maximum of both of the unnormalized and normalized (by wavenumber 0, i.e., azimuthal mean rain rates) wavenumber 1 asymmetries of all four types of precipitation is located mainly in the down motion quadrants, consistent with many previous studies (Burpee & Black, 1989; CKM06; Frank & Ritchie, 1999; LMC04; Marks, 1985; Miller, 1958; Shapiro, 1983; Reasor et al., 2000; Willoughby et al., 1984).

By adding wavenumbers 2–6 to wavenumber 1 in this study, it is found that the phase maximum of the motion-relative wavenumber 1–6 asymmetry shifts cyclonically around the TC center in all cases including four types of precipitation, five TC-prone basins, three TC intensity groups, and slow and fast TC motion groups (Figures 4–8). This is similar to Kepert and Wang (2001) who found that the nonlinear representation will induce a cyclonic rotation of the phase maximum of precipitation asymmetry relative to the linear result in Shapiro (1983). As TC intensity increases, the phase maximum of normalized motion-relative wavenumber 1 and wavenumber 1–6 asymmetries of total precipitation shifts cyclonically from down motion for both tropical storms and Categories 1–2 hurricanes to down motion right for major hurricanes (Figures 7 and 8). For TSs with different motion speeds, the asymmetry index for fast motion cases is about twice as high as that for slow motion cases (Table 6). Asymmetry indices of motion-relative wavenumber 1 and wavenumber 1–6 asymmetries of total precipitation are the highest for CAT1-2 hurricanes, which is higher than that of tropical storms and major hurricanes (Table 5). This supports the hypothesis that the asymmetry of vortex and rainfall field of Categories 1 and 2 hurricanes is more affected by the motion factor than that of tropical storms or major hurricanes (Klotz & Jiang, 2016).

In the shear-relative framework, it is found that the phase maximum of normalized wavenumber 1 and wavenumber 1–6 asymmetries of total precipitation is clearly downshear left in the NH and downshear right in the SH basins (Figures 9 and 10), consistent with many previous studies (e.g., Corbosiero & Molinari, 2002; CKM06; Cecil, 2007; Ueno, 2007; Wingo & Cecil, 2010). The asymmetry index of wavenumber 1 and wavenumber 1–6 asymmetries of total precipitation relative to the vertical wind shear is about 2 to 3 times as large as that relative to the storm motion (Tables 4 and 7). In agreement with CKM06, our results strongly suggest that the vertical wind shear is a more important factor in producing the precipitation asymmetry. Adding higher wavenumbers also increases the shear-relative asymmetry index by about 9–30% (Tables 8 and 9). In general, the total precipitation of TCs in SH basins are more asymmetric than that in ATL, EPA, and NWP basins in both the shear-relative (Table 6) and motion-relative (Table 4) frameworks. Asymmetry indices of shear-relative wavenumber 1 and wavenumber 1–6 asymmetries of total precipitation under high shear are a factor of 1.5 higher than those under moderate shear, which are twice as high as those under low shear. Asymmetry indices of shear-relative wavenumber 1 and wavenumber 1–6 asymmetries of total precipitation decrease as TC intensity increases for both low, moderate, and high shear conditions.

To examine the combined effect of storm motion and vertical wind shear to the TC rainfall asymmetry, the samples are grouped into 24 subgroups such that the shear vectors are in the same, opposite, right, and left

of the TC motion directions, and by the strength of the shear value and the motion speed. A dominant downshear left wavenumber 1 asymmetry maximum is found regardless of the shear vector orientation to the TC motion, the magnitude of the shear value, and the speed of TC motion (Figures 13 and 14). This is consistent with CKM06 and indicates that the shear effect is dominant over the motion effect for determining the wavenumber 1 rainfall asymmetry. However, after adding wavenumber 2–6 components, the maximum asymmetry of wavenumber 1–6 asymmetry becomes downshear right for the subgroup with low shear, fast motion, and the shear vector left to the motion (Figure 15ld). This indicates that when the shear is low and the motion speed is fast, the motion-induced down motion left component of wavenumbers 1–6 becomes a more important factor. For all other subgroups, the phase maximum of wavenumber 1–6 asymmetry is still downshear left. Asymmetry amplitudes of both wavenumber 1 and wavenumber 1–6 asymmetries are the largest when the shear and motion vectors are in the same directions and the smallest when they are opposite due to the combination of motion-induced down motion to down motion left and the shear-induced downshear-left components (Table 9).

Acknowledgments
The TRMM data have been provided by the Goddard Earth Sciences (GES) Data and Information Services Center (DISC) Distributed Active Archive Center (DAAC; http://disc.sci.gsfc.nasa.gov/TRMM), and the Tropical Cyclone Best Track Data have been provided by the U.S. Navy's Joint Typhoon Warning Center (JTWC; https://pzal.ndbc.noaa.gov/collab/jtwc/). The data used in this study are listed in the references, tables, and figures. The authors thank Jonathan Zawislak, Bradley Klotz, Ping Zhu, and Hugh Willoughby for helpful insights and discussions on this work. Thanks are also due to Joseph Zagrodnik, Micheal Fischer, and Cheng Tao for TRMM data processing assistance. Thanks to three anonymous reviewers, whose comments and suggestions help improve the manuscript substantially. This research was supported by NASA Earth and Space Science Fellowship (NESSF) award NNX14AL33H. Additional support was provided by NOAA Joint Hurricane Testbed (JHT) grants NA11OAR4310193, NA13OAR4590191, NA15OAR4590199, and NA17OAR4590142 under the direction of Chris Landsea and NASA New Investigator Program (NIP) award NNX10AG55G, NASA Hurricane Science Research Program (HSRP) award NNX10AG34G, and NASA Weather And Atmospheric Dynamics (WAAD) award NNX17AH72G under the direction of Ramesh Kakar and Ming-Ying Wei.

References

Alvey, G. R. III, Zawislak, J., & Zipser, E. (2015). Precipitation properties observed during tropical cyclone intensity change. *Monthly Weather Review*, *143*(11), 4476–4492. https://doi.org/10.1175/MWR-D-15-0065.1

Burpee, R. W., & Black, M. L. (1989). Temporal and spatial variations of rainfall near the centers of two tropical cyclones. *Monthly Weather Review*, *117*(10), 2204–2218. https://doi.org/10.1175/1520-0493(1989)117%3C2204:TASVOR%3E2.0.CO;2

Cecil, D. J. (2007). Satellite-derived rain rates in vertically sheared tropical cyclones. *Geophysical Research Letters*, *34*, L02811. https://doi.org/10.1029/2006GL027942

Chen, S. S., Knaff, J. A., & Marks, F. D. Jr. (2006). Effects of vertical wind shear and storm motion on tropical cyclone rainfall asymmetries deduced from TRMM. *Monthly Weather Review*, *134*(11), 3190–3208. https://doi.org/10.1175/MWR3245.1

Corbosiero, K. L., & Molinari, J. (2002). The effects of vertical wind shear on the distribution of convection in tropical cyclones. *Monthly Weather Review*, *130*(8), 2110–2123. https://doi.org/10.1175/1520-0493(2002)130%3C2110:TEOVWS%3E2.0.CO;2

Corbosiero, K. L., & Molinari, J. (2003). The relationship between storm motion, vertical wind shear, and convective asymmetries in tropical cyclones. *Journal of the Atmospheric Sciences*, *60*(2), 366–376. https://doi.org/10.1175/1520-0469(2003)060%3C0366:TRBSMV%3E2.0.CO;2

DeMaria, M., DeMaria, R. T., Knaff, J. A., & Molenar, D. (2012). Tropical cyclone lightning and rapid intensity change. *Monthly Weather Review*, *140*(6), 1828–1842. https://doi.org/10.1175/MWR-D-11-00236.1

Frank, W. M. (1977). Convective fluxes in tropical cyclones. *Journal of the Atmospheric Sciences*, *34*(10), 1554–1568. https://doi.org/10.1175/1520-0469(1977)034%3C1554:CFITC%3E2.0.CO;2

Frank, W. M., & Ritchie, E. A. (1999). Effects of environmental flow upon tropical cyclone structure. *Monthly Weather Review*, *127*(9), 2044–2061. https://doi.org/10.1175/1520-0493(1999)127%3C2044:EOEFUT%3E2.0.CO;2

Jiang, H., Liu, C., & Zipser, E. J. (2011). A TRMM-based tropical cyclone cloud and precipitation feature database. *Journal of Applied Meteorology and Climatology*, *50*(6), 1255–1274. https://doi.org/10.1175/2011JAMC2662.1

Jiang, H., Ramirez, E. M., & Cecil, D. J. (2013). Convective and rainfall properties of tropical cyclone inner cores and rainbands from 11 years of TRMM data. *Monthly Weather Review*, *141*(2), 431–450. https://doi.org/10.1175/MWR-D-11-00360.1

Jiang, H., & Zipser, E. J. (2010). Contribution of tropical cyclones to the global precipitation from eight seasons of TRMM data: Regional, seasonal, and interannual variations. *Journal of Climate*, *23*(6), 1526–1543. https://doi.org/10.1175/2009JCLI3303.1

Kepert, J., & Wang, Y. (2001). The dynamics of boundary layer jets within the tropical cyclone core. Part II: Nonlinear enhancement. *Journal of the Atmospheric Sciences*, *58*(17), 2485–2501. https://doi.org/10.1175/1520-0469(2001)058%3C2485:TDOBLJ%3E2.0.CO;2

Klotz, B. W., & Jiang, H. (2016). Global composites of surface wind speeds in tropical cyclones based on a 12 year scatterometer database. *Geophysical Research Letters*, *43*, 10,480–10,488. https://doi.org/10.1002/2016GL071066

Kummerow, C., Hong, Y., Olson, W. S., Yang, S., Adler, R. F., McCollum, J., et al. (2001). The evolution of the Goddard Profiling Algorithm (GPROF) for rainfall estimation from passive microwave sensors. *Journal of Applied Meteorology*, *40*(11), 1801–1820. https://doi.org/10.1175/1520-0450(2001)040%3C1801:TEOTGP%3E2.0.CO;2

Lonfat, M., Marks, F. D. Jr., & Chen, S. S. (2004). Precipitation distribution in tropical cyclones using the Tropical Rainfall Measuring Mission (TRMM) microwave imager: A global perspective. *Monthly Weather Review*, *132*(7), 1645–1660. https://doi.org/10.1175/1520-0493(2004)132%3C1645:PDITCU%3E2.0.CO;2

Lonfat, M., Rogers, R., Marchok, T., & Marks, F. D. Jr. (2007). A parametric model for predicting hurricane rainfall. *Monthly Weather Review*, *135*(9), 3086–3097. https://doi.org/10.1175/MWR3433.1

Marks, F. D. Jr. (1985). Evolution of the structure of precipitation in Hurricane Allen (1980). *Monthly Weather Review*, *113*(6), 909–930. https://doi.org/10.1175/1520-0493(1985)113%3C0909:EOTSOP%3E2.0.CO;2

Marks, F. D. Jr., & Houze, R. A. Jr. (1987). Inner core structure of Hurricane Alicia from airborne Doppler radar observations. *Journal of the Atmospheric Sciences*, *44*(9), 1296–1317. https://doi.org/10.1175/1520-0469(1987)044%3C1296:ICSOHA%3E2.0.CO;2

Miller, B. I. (1958). On the maximum intensity of hurricanes. *Journal of Meteorology*, *15*(2), 184–195. https://doi.org/10.1175/1520-0469(1958)015%3C0184:OTMIOH%3E2.0.CO;2

Montgomery, M. T., Nicholls, M. E., Cram, T. A., & Saunders, A. B. (2006). A vortical hot tower route to tropical cyclogenesis. *Journal of the Atmospheric Sciences*, *63*(1), 355–386. https://doi.org/10.1175/JAS3604.1

Montgomery, M. T., & Smith, R. K. (2011). Paradigms for tropical-cyclone intensification. NAVAL POSTGRADUATE SCHOOL MONTEREY CA DEPT OF METEOROLOGY.

Nolan, D. S., Moon, Y., & Stern, D. P. (2007). Tropical cyclone intensification from asymmetric convection: Energetics and efficiency. *Journal of the Atmospheric Sciences*, *64*(10), 3377–3405. https://doi.org/10.1175/JAS3988.1

Olson, W. S., Kummerow, C. D., Heymsfield, G. M., & Giglio, L. (1996). A method for combined passive–active microwave retrievals of cloud and precipitation profiles. *Journal of Applied Meteorology*, *35*(10), 1763–1789. https://doi.org/10.1175/1520-0450(1996)035%3C1763:AMFCPM%3E2.0.CO;2

Ooyama, K. (1969). Numerical simulation of the life cycle of tropical cyclones. *Journal of the Atmospheric Sciences*, *26*(1), 3–40. https://doi.org/10.1175/1520-0469(1969)026%3C0003:NSOTLC%3E2.0.CO;2

Powell, M. D. (1980). Evaluations of diagnostic marine boundary-layer models applied to hurricanes. *Monthly Weather Review*, *108*(6), 757–766. https://doi.org/10.1175/1520-0493(1980)108%3C0757:EODMBL%3E2.0.CO;2

Powell, M. D., Vickery, P. J., & Reinhold, T. A. (2003). Reduced drag coefficient for high wind speeds in tropical cyclones. *Nature*, *422*(6929), 279–283. https://doi.org/10.1038/nature01481

Reasor, P. D., & Eastin, M. D. (2012). Rapidly intensifying hurricane Guillermo (1997). Part II: Resilience in shear. *Monthly Weather Review*, *140*(2), 425–444. https://doi.org/10.1175/MWR-D-11-00080.1

Reasor, P. D., Eastin, M. D., & Gamache, J. F. (2009). Rapidly intensifying Hurricane Guillermo (1997). Part I: Low-wavenumber structure and evolution. *Monthly Weather Review*, *137*(2), 603–631. https://doi.org/10.1175/2008MWR2487.1

Reasor, P. D., Montgomery, M. T., Marks, F. D. Jr., & Gamache, J. F. (2000). Low-wavenumber structure and evolution of the hurricane inner core observed by airborne dual-Doppler radar. *Monthly Weather Review*, *128*(6), 1653–1680. https://doi.org/10.1175/1520-0493(2000)128%3C1653:LWSAEO%3E2.0.CO;2

Reasor, P. D., Rogers, R., & Lorsolo, S. (2013). Environmental flow impacts on tropical cyclone structure diagnosed from airborne Doppler radar composites. *Monthly Weather Review*, *141*(9), 2949–2969. https://doi.org/10.1175/MWR-D-12-00334.1

Rodgers, E. B., Chang, S. W., & Pierce, H. F. (1994). A satellite observational and numerical study of precipitation characteristics in western North Atlantic tropical cyclones. *Journal of Applied Meteorology*, *33*(2), 129–139. https://doi.org/10.1175/1520-0450(1994)033%3C0129:ASOANS%3E2.0.CO;2

Rogers, R., Chen, S., Tenerelli, J., & Willoughby, H. (2003). A numerical study of the impact of vertical shear on the distribution of rainfall in Hurricane Bonnie (1998). *Monthly Weather Review*, *131*(8), 1577–1599. https://doi.org/10.1175//2546.1

Shapiro, L. J. (1983). The asymmetric boundary layer flow under a translating hurricane. *Journal of the Atmospheric Sciences*, *40*(8), 1984–1998. https://doi.org/10.1175/1520-0469(1983)040%3C1984:TABLFU%3E2.0.CO;2

Shapiro, L. J., & Willoughby, H. E. (1982). The response of balanced hurricanes to local sources of heat and momentum. *Journal of the Atmospheric Sciences*, *39*(2), 378–394. https://doi.org/10.1175/1520-0469(1982)039%3C0378:TROBHT%3E2.0.CO;2

Simmons, A., Uppala, S., Dee, D., & Kobayashi, S. (2006). ERA-Interim: New ECMWF reanalysis products from 1989 onwards. *ECMWF Newsletter*, *110*, 25–36.

Stull, R. B. (1987). *An introduction to boundary layer meteorology* (p. 666). Berlin, Germany: Springer.

Tao, C., & Jiang, H. (2015). Distributions of shallow to very deep precipitation–convection in rapidly intensifying tropical cyclones. *Journal of Climate*, *28*(22), 8791–8824. https://doi.org/10.1175/JCLI-D-14-00448.1

Tao, C., Jiang, H., & Zawislak, J. (2017). The relative importance of stratiform and convective rainfall in rapidly intensifying tropical cyclones. *Monthly Weather Review*, *145*(3), 795–809. https://doi.org/10.1175/MWR-D-16-0316.1

Ueno, M. (2007). Observational analysis and numerical evaluation of the effects of vertical wind shear on the rainfall asymmetry in the typhoon inner-core region. *Journal of the Meteorological Society of Japan Series II*, *85*(2), 115–136. https://doi.org/10.2151/jmsj.85.115

Willoughby, H. E., Marks, F. D. Jr., & Feinberg, R. J. (1984). Stationary and moving convective bands in hurricanes. *Journal of the Atmospheric Sciences*, *41*(22), 3189–3211. https://doi.org/10.1175/1520-0469(1984)041%3C3189:SAMCBI%3E2.0.CO;2

Wingo, M. T., & Cecil, D. J. (2010). Effects of vertical wind shear on tropical cyclone precipitation. *Monthly Weather Review*, *138*(3), 645–662. https://doi.org/10.1175/2009MWR2921.1

Yu, Z., Wang, Y., & Xu, H. (2015). Observed rainfall asymmetry in tropical cyclones making landfall over China. *Journal of Applied Meteorology and Climatology*, *54*(1), 117–136. https://doi.org/10.1175/JAMC-D-13-0359.1

Zagrodnik, J. P., & Jiang, H. (2014). Rainfall, convection, and latent heating distributions in rapidly intensifying tropical cyclones. *Journal of the Atmospheric Sciences*, *71*(8), 2789–2809. https://doi.org/10.1175/JAS-D-13-0314.1

Zhu, P., Menelaou, K., & Zhu, Z. (2014). Impact of subgrid-scale vertical turbulent mixing on eyewall asymmetric structures and mesovortices of hurricanes. *Quarterly Journal of the Royal Meteorological Society*, *140*(679), 416–438. https://doi.org/10.1002/qj.2147